Monthly Notices
of the
ROYAL ASTRONOMICAL SOCIETY

MNRAS **470,** 688–705 (2017) doi:10.1093/mnras/stx1209
Advance Access publication 2017 May 18

Improving Fisher matrix forecasts for galaxy surveys: window function, bin cross-correlation and bin redshift uncertainty

Alberto Bailoni,⋆ Alessio Spurio Mancini⋆ and Luca Amendola
Institut für Theoretische Physik, Ruprecht-Karls-Universität Heidelberg, Philosophenweg 16, D-69120 Heidelberg, Germany

Accepted 2017 May 15. Received 2017 May 3; in original form 2016 September 21

ABSTRACT

The Fisher matrix is a widely used tool to forecast the performance of future experiments and approximate the likelihood of large data sets. Most of the forecasts for cosmological parameters in galaxy clustering studies rely on the Fisher matrix approach for large-scale experiments like DES, Euclid or SKA. Here, we improve upon the standard method by taking into account three effects: the finite window function, the correlation between redshift bins and the uncertainty on the bin redshift. The first two effects are negligible only in the limit of infinite surveys. The third effect, in contrast, is negligible for infinitely small bins. Here, we show how to take into account these effects and what the impact on forecasts of a *Euclid*-type experiment will be. The main result of this paper is that the windowing and the bin cross-correlation induce a considerable change in the forecasted errors, of the order of 10–30 per cent for most cosmological parameters, while the redshift bin uncertainty can be neglected for bins smaller than $\Delta z = 0.1$ roughly.

Key words: methods: statistical – surveys – galaxies: statistics – cosmological parameters – large-scale structure of Universe.

1 INTRODUCTION

An important task of cosmology is to study the composition and evolution of the Universe. Different models have been introduced, which rely on cosmological parameters like the Hubble constant, the primordial scalar spectral index, and matter abundances. From a theoretical perspective, it is crucial to distinguish between different models and determine which of them provide the closest approximations to the observed data. In a few years, large-scale surveys like Euclid (Laureijs et al. 2011), DESI (DESI Collaboration 2016), HETDEX (Hill et al. 2008), eBOSS (eBOSS Collaboration 2016), BigBOSS (Schlegel et al. 2011), DES (Flaugher 2005), Pan-STARRS (Kaiser et al. 2002), LSST (LSST Science Collaboration et al. 2009) and SKA (Yahya et al. 2015) will provide huge data sets containing information on galaxy positions at high redshift. The data will allow us to study how the observed clustering of galaxies evolves over time, and how the gravitational lensing is generated by large-scale structures in the Universe. The data will be mainly encoded in 3D or angular power spectra and in higher order moments, since these descriptors are usually the direct outcome of cosmological theories. The data will then be combined with the cosmic microwave background, in particular, with the *Planck* satellite (Planck Collaboration XIII 2016).

The first attempt to characterize large-scale structure and measure the power spectrum from data was presented in Yu & Peebles (1969) and Groth & Peebles (1977). In Baumgart & Fry (1991), the result was generalized for redshift surveys and full three-dimensional (3D) galaxy positions. In 1994, Feldman, Kaiser & Peacock (1994) provided an estimate of the power spectrum and, in a following pioneering paper, Tegmark (1997a) introduced an optimal method for estimating the power spectrum based on Bayesian statistics and the Fisher matrix formalism (Fisher 1935).

Given the measured power spectrum, a maximum likelihood analysis yields then the best estimate of the parameters, characterizing the theoretical power spectrum, and the first attempts to apply this method at linear scales were made by Fisher, Scharf & Lahav (1994) and Heavens & Taylor (1995). To formalize the theoretical power spectrum, the most commonly employed methods are the following two: The first uses real space coordinates, whereas the second expresses the power spectrum in angular coordinates and redshift space, so that it is directly related to the observable angular correlation function. The latter method is based on a spherical harmonic decomposition of the projected density in redshift shells, as shown in Heavens & Taylor (1995) (for recent applications, see Montanari & Durrer 2012, 2015; Bonaldi et al. 2016; Raccanelli et al. 2016). In this approach, one has the important advantage that large-scale relativistic effects, for example,

⋆E-mail: bailoni@thphys.uni-heidelberg.de (AB); spuriomancini@thphys.uni-heidelberg.de (ASM)

lensing, are straightforwardly included, as well as correlations between different shells. On the other hand, the 3D nature of the correlation is compressed into a set of 2D projections and some information is then lost. This information is completely recovered in the limit of an infinite redshift resolution along the line of sight, when the two power spectrum formalizations become equivalent.

Even before performing large-scale surveys, when data are not available yet, it is important to know which set-up will allow us to optimally distinguish between theoretical models with different parameters. Given the specifications of the survey and the model, we can compute the probability distributions of the parameters that define the model by using Bayesian statistics and the Fisher matrix formalism. Such predictions, called *forecasts*, are crucial for setting up a survey and defining the models to focus on. If the survey is still in the design phase, then several survey-specific parameters can also be included in the forecast, for example, the density of galaxies, redshift errors, the survey's depth and sky coverage.

Analysing a large data set of 3D galaxy positions in an expanding universe is time-consuming. The standard procedure for a galaxy redshift survey is to divide the survey space in N redshift bins, so that each bin represents data from a different cosmological epoch. This can be formalized by introducing the concept of a top-hat survey-bin window function $W_i(\boldsymbol{x})$, such that $\int W_i(\boldsymbol{x})\mathrm{d}^3x = V_i$ and $W_i(\boldsymbol{x})$ is equal to 1 inside the ith survey-bin V_i and 0 otherwise. Most of the forecast studies based on a real-space description of the power spectrum (e.g. Seo & Eisenstein 2003; Amendola et al. 2005; Wang 2006; Albrecht et al. 2009; Di Porto et al. 2012; Wang 2012; Xu et al. 2014) typically imply several assumptions, four of which are spelled out now. The first assumption is that the power spectrum computed for a finite redshift bin volume is not significantly different from the power spectrum computed with respect to the full sky, i.e. the window function effect on the matter power spectrum can be neglected. The second assumption is that the bin cross-correlation spectra can be ignored, i.e. only correlations between galaxies from the same redshift bins are considered. Thirdly, the cross-correlations among different k-modes, arising because of the finiteness of the survey volume, are also neglected. Whereas for an infinite survey these assumptions would hold, they have never been properly evaluated for a finite survey.[1] The fourth assumption is that one can assign to the z-dependent functions, for example, the growth rate, the growth function, the bias, the Hubble function, etc., a precise redshift value, usually taken to be the median redshift of the bin. This is an approximation that will also be discussed later on.

In this paper, we focus on forecast studies for galaxy clustering surveys and test how well the above assumptions hold for future surveys, in particular, the Euclid survey. Our first contribution is the formalization of the effect of the window function, the bin cross-correlations and the bin redshift uncertainty; although we focus on forecast studies, this theoretical description can also contribute to parameter estimation when data are available. As the second contribution, we quantify the effects of the related assumptions by comparing the forecast confidence regions for the cosmological parameters computed with and without each of the mentioned assumptions. Given the specifications of the planned Euclid survey, we investigate how these effects depend on the number of redshift bins. Then, we study how to introduce the Alcock–Paczynski (AP) effect (Alcock & Paczyński 1979). We compute the windowed and the cross-correlation spectra using a Fast Fourier Transform (FFT) algorithm (Press 2007). Its output is further processed using an optimized Fisher matrix implementation, which we make publicly available.[2] The main result of this paper is that the window function effect increases the uncertainties because it flattens out the signal, while numerically we find that the bin cross-correlation reduces them (see Section 5.1); the combined effect induces a sizable *increase* in the forecasted errors, of the order of 10–30 per cent for most cosmological parameters. Finally, the bin redshift uncertainty always increases the overall uncertainty, but it is important only for bins larger than $\Delta z \approx 0.1$.

The structure of this paper is as follows: In Section 2, we briefly introduce the relevant theoretical concepts related to the linear matter power spectrum and redshift distortions, focusing on the Lambda cold dark matter (ΛCDM) model. In Section 3, we overview the Fisher matrix approach, the effects of the window function, the bin cross-correlations and the bin redshift uncertainty. In Section 4, we describe how to include the effects of the redshift distortions in the convolved and cross-correlation spectra and tune the parameters of the radial FFT algorithm based on analytical power spectra. In Section 5, we discuss the results we obtained. Section 6 sums up this paper.

2 THE OBSERVED MATTER POWER SPECTRUM

In this section, we will briefly introduce the theoretical concepts regarding the linear matter power spectrum, the relevant cosmological quantities and the redshift distortions. Let us first define the ensemble-averaged power spectrum $P(\boldsymbol{k})$ of a survey in a volume V:

$$V\left\langle \delta_k \delta^*_{k'} \right\rangle \equiv \frac{(2\pi)^3}{V} P(\boldsymbol{k})\delta_{\mathrm{D}}(\boldsymbol{k}-\boldsymbol{k}'), \tag{1}$$

where δ_k are the Fourier coefficients of the density contrast $\delta(\boldsymbol{x})$ and $\delta_{\mathrm{D}}(\boldsymbol{k})$ is the Dirac delta. The shell volume V comes from the normalization convention for the 3D Fourier transform of a generic function $f(\boldsymbol{x})$:

$$f(\boldsymbol{x}) = \frac{V}{(2\pi)^3}\int f_k \mathrm{e}^{i\boldsymbol{k}\cdot\boldsymbol{x}}\mathrm{d}^3k, \tag{2}$$

$$f_k = \frac{1}{V}\int f(\boldsymbol{x})\mathrm{e}^{-i\boldsymbol{k}\cdot\boldsymbol{x}}\mathrm{d}^3k. \tag{3}$$

[1] Note that for a power spectrum expressed in redshift space, cross-correlation spectra and window function effects have already been taken into account with lensing effects included (Montanari & Durrer 2015).

[2] https://github.com/abailoni/fisher-correlations

The data power spectrum is a single sampling of the distribution. Nevertheless, when an average on the theoretical prediction is considered, an ensemble average and a sample average are equivalent, assuming that the survey is a fair example of the universe (Amendola & Tsujikawa 2010). Given equation (1), it follows that for equal wave vectors, the power spectrum is $P(\boldsymbol{k}) = V\langle\delta_{\boldsymbol{k}}\delta_{-\boldsymbol{k}}\rangle$.[3] If the field is then assumed to be isotropic, the power spectrum will depend only on the modulus k.

We assume a flat, homogeneous and isotropic metric. Then, neglecting the small contribution given by radiation, the Hubble parameter $H(z)$ is

$$H(z) = H_0\sqrt{\Omega_{\rm m}^{(0)}(1+z)^3 + \Omega_{\rm DE}^{(0)}\exp\left[3\int_0^z \frac{1+w(z')}{1+z'}{\rm d}z'\right]}, \tag{4}$$

where $\Omega_i^{(0)}$ is the present fraction of the critical density in the form of component i, which can be radiation (r), matter (m), baryonic matter (b), cold dark matter (cdm), curvature (k) and dark energy (DE). The dark energy parameter $w(z) = w_0$ is a constant in the ΛCDM model. The mass density $\Omega_{\rm m}(z)$ at a generic redshift is given by

$$\Omega_{\rm m}(z) = \frac{\Omega_{\rm m}^{(0)}(1+z)^3}{(H(z)/H_0)^2} \tag{5}$$

and $\Omega_{\rm DE}^{(0)} = 1 - \Omega_{\rm m}^{(0)}$. The angular diameter distance $D_{\rm A}(z)$ expressed in units of Mpc is

$$D_{\rm A}(z) = \frac{c}{1+z}\int_0^z \frac{{\rm d}z'}{H(z')} \tag{6}$$

and the growth function $G(k, z)$ is

$$G(k, z) = \frac{\delta_{\rm m}(k, z)}{\delta_{\rm m}(k, 0)}, \tag{7}$$

where $\delta_{\rm m}(k, z)$ is the matter density at a certain redshift and scale. The growth rate is $f(k, z) \equiv \dot{\delta}_{\rm m}(k, z)/(H(z)\delta_{\rm m}(k, z))$, and in the ΛCDM model, it can be approximated as scale independent, $f(z) = \Omega_{\rm m}^{\gamma}(z)$ (Peebles 1976; Lahav et al. 1991; Linder 2005; Polarski & Gannouji 2008), where $\gamma \simeq 0.55$ (Peebles 1980; Wang & Steinhardt 1998).

Given the set of cosmological parameters $\boldsymbol{\theta} = \{h, n_{\rm s}, \Omega_{\rm b}^{(0)}, \Omega_{\rm cdm}^{(0)}, w_0\}$, the linear matter power spectrum at a redshift z can then be written as (Amendola & Tsujikawa 2010)

$$P(k, z; \boldsymbol{\theta}) = A_{\rm s}\, k^{q(n_{\rm s})}\, T^2(k; \boldsymbol{\theta})\, G^2(k, z; \boldsymbol{\theta}), \tag{8}$$

where $A_{\rm s}$ is the amplitude of the spectrum, $q(n_{\rm s})$ is a function of the spectral index $n_{\rm s}$, and $T(k; \boldsymbol{\theta})$ is the transfer function that, in a linear regime and in the ΛCDM model, does not depend on redshift. Note that from now on, we highlight the dependence of the quantities $H(z; \boldsymbol{\theta})$, $D_{\rm A}(z; \boldsymbol{\theta})$, $G^2(k, z; \boldsymbol{\theta})$ and $f(k, z; \boldsymbol{\theta})$ on the set $\boldsymbol{\theta}$ of cosmological parameters.

Since we observe the galaxy distribution in redshift space and not observe directly the matter density in real space, we have to take into account the bias and the redshift distortion. If we define the linear bias as $\delta_{k,\,\rm matter} \cdot b(z, k) \equiv \delta_{k,\,\rm galaxies}$ and normalize the power spectrum to σ_8, then the following equation follows:

$$\delta_{\rm obs}(k, \mu) = \sigma_8 b(k, z)\left[1 + \frac{f(k, z; \boldsymbol{\theta})}{b(k, z; \boldsymbol{\theta})}\mu^2\right]\delta_k, \tag{9}$$

where μ is the cosine of the angle between $\boldsymbol{k}$ and the line of sight. Although, in this form, the redshift distortion is valid only in the flat-sky approximation, we apply it to a large-sky survey as Euclid, following most of previous forecast works. The quantities $G(k, z; \boldsymbol{\theta})$, $b(k, z)$ and $f(k, z; \boldsymbol{\theta})$ are, in general, scale-dependent. Note that the redshift distortions lead to an anisotropic observed power spectrum. Finally, we can consider a scale-independent residual shot-noise term $P_{\rm s}(z)$ on top of the shot noise $1/n_{\rm gal}(z)$, where $n_{\rm gal}(z)$ is the number density of galaxies. This term is added in the case of incomplete removal of the shot noise arising from the discrete sampling of galaxies. Thus, the final expression is (Seo & Eisenstein 2003)

$$P_{\rm obs}(k, \mu, z; \boldsymbol{\theta}) = P_{\rm s}(z) + \sigma_8^2 b^2(k, z)\left[1 + \beta(k, z; \boldsymbol{\theta})\mu^2\right]^2 P(k, z; \boldsymbol{\theta}), \tag{10}$$

where we defined $\beta(k, z; \boldsymbol{\theta}) \equiv f(k, z; \boldsymbol{\theta})/b(k, z)$. We will consider b to be scale independent and, since the bias function is undefined along with the parameters above, we add a bias parameter for each bin and marginalize over it (see Seo & Eisenstein 2003 and Section 6), assuming a uniform prior.

If the set of parameters $\boldsymbol{\theta}$ represents our fiducial cosmological model, varying it to a new set $\boldsymbol{\theta}'$ not only changes the shape and amplitude of the spectrum, because the transfer and growth functions $T(k; \boldsymbol{\theta})$ and $G(k, z; \boldsymbol{\theta})$ are different, but new distortions are introduced in the vector $\boldsymbol{k}$ and the volume in which the spectrum is computed. By taking into account these modifications, called the AP effect, the observed spectrum can be formalized as (Alcock & Paczyński 1979; Seo & Eisenstein 2003; Amendola & Tsujikawa 2010)

$$P_{\rm obs}(k, \mu, z; \boldsymbol{\theta}) = P_{\rm s}(z) + \frac{H(z; \boldsymbol{\theta}') \cdot D_{\rm A}^2(z; \boldsymbol{\theta})}{H(z; \boldsymbol{\theta}) \cdot D_{\rm A}^2(z; \boldsymbol{\theta}')}\sigma_8^2 b^2(k, z)\left[1 + \beta(k, z; \boldsymbol{\theta}')\mu_{\boldsymbol{\theta}'}^2\right]^2 P(k_{\boldsymbol{\theta}'}, z; \boldsymbol{\theta}'). \tag{11}$$

[3] Note that since $\delta(\boldsymbol{x})$ is real, then $\delta_{\boldsymbol{k}}^* = \delta_{-\boldsymbol{k}}$.

The transformations of $k = |\boldsymbol{k}|$ and μ are given by the following equations:

$$k_{\theta'} = \Upsilon\, k, \tag{12}$$

$$\mu_{\theta'} = \frac{H(z;\boldsymbol{\theta}')\mu}{H(z;\boldsymbol{\theta})\Upsilon}, \tag{13}$$

where

$$\Upsilon = \frac{\sqrt{H^2(z;\boldsymbol{\theta}')D_{\rm A}^2(z;\boldsymbol{\theta}')\mu^2 - H^2(z,\boldsymbol{\theta})D_{\rm A}^2(z;\boldsymbol{\theta})[\mu^2-1]}}{H(z;\boldsymbol{\theta})D_{\rm A}(z;\boldsymbol{\theta}')}. \tag{14}$$

Now that we have *introduced* the observed matter power spectrum, we will analyse how it is affected by the introduction of a window function and the bin cross-correlations.

3 WINDOW FUNCTION EFFECT, CORRELATIONS BETWEEN BINS AND BIN REDSHIFT UNCERTAINTY

3.1 Fisher information matrix for correlated bins

In the Fisher information matrix approach (Fisher 1935; Tegmark, Taylor & Heavens 1997), the Fourier coefficients $\delta_{\boldsymbol{k}}$ of the density contrast are random variables, which are expected to have a Gaussian distribution in the standard model of inflation, as long as they remain linear (Lyth & Liddle 2009). If we call $\boldsymbol{\theta}$ the set of cosmological parameters, then the likelihood is $P(\delta_{\boldsymbol{k}}|\boldsymbol{\theta})$. By applying Bayes' theorem with an uniform prior, we obtain the posterior probability $\mathcal{L}(\boldsymbol{\theta}|\delta_{\boldsymbol{k}}) \propto P(\delta_{\boldsymbol{k}}|\boldsymbol{\theta})$, now viewed as a function of the parameters (for a detailed review of this and what follows, see Heavens 2009; Trotta 2008; Dodelson 2003; Amendola & Tsujikawa 2010). The probability $\mathcal{L}(\boldsymbol{\theta}|x)$ is also commonly called likelihood, so we will also follow this notation. The Fisher matrix method approximates such likelihood $\mathcal{L}(\boldsymbol{\theta}|x)$ around its peak by a Gaussian-correlated distribution of parameters $\boldsymbol{\theta}$. The Fisher matrix is defined as the inverse of the parameter covariance matrix of the distribution and it encodes then the Gaussian uncertainties $\sigma_{\boldsymbol{\theta}}$ on the parameters. The maximum of $\mathcal{L}(\boldsymbol{\theta}|x)$ can be found using efficient numerical algorithms, for example, Newton–Raphson (Press 2007), and the symmetric Fisher matrix can be obtained by sampling $\mathcal{L}(\boldsymbol{\theta}|\delta_{\boldsymbol{k}})$ $2N_{\boldsymbol{\theta}}$ times, where $N_{\boldsymbol{\theta}}$ is the number of parameters. Here, we will use the Fisher matrix tools to propagate the uncertainties on the cosmological parameters when data are not available yet, i.e. when we are *forecasting a future galaxy redshift survey*. This is possible because in a forecast, we can fix the maximum of $\mathcal{L}(\boldsymbol{\theta}|\delta_{\boldsymbol{k}})$ at the fiducial cosmological parameters $\boldsymbol{\theta}_0$ given by previous data.

The standard Fisher matrix approach typically employed in forecast studies for galaxy clustering is the following (Seo & Eisenstein 2003). After dividing the survey space in N redshift bins along the line of sight, a set of N coefficients $\boldsymbol{\delta}_{\boldsymbol{k}} = \{\delta_{\boldsymbol{k}}^{(1)}, \ldots, \delta_{\boldsymbol{k}}^{(N)}\}$ is deduced from the data. All the redshift-dependent quantities, for example, $G(z;\boldsymbol{\theta})$, $b(z)$and $f(z;\boldsymbol{\theta})$, are taken at the median bin redshift (from now on, we ignore their possible k-dependence). The random variables assigned to the coefficients are statistically independent because bin cross-correlation spectra $V\langle\delta_{\boldsymbol{k}}^{(i)}\delta_{-\boldsymbol{k}}^{(j)}\rangle$ for $i \neq j$ are ignored and set to zero. Also, the effects of the window function are neglected; thus, the observed power spectrum in equation (11) for each bin i is $V\langle\delta_{\boldsymbol{k}}^{(i)}\delta_{-\boldsymbol{k}}^{(i)}\rangle \stackrel{!}{=} P(k,\mu,z_i)$. The definition of the power spectrum in equation (1) shows that modes at different wave vectors $\boldsymbol{k}$ are independent if we assume an homogeneous field, i.e. $\langle\delta_{\boldsymbol{k}}\delta_{-\boldsymbol{k}'}\rangle = 0$ for $\boldsymbol{k} \neq \boldsymbol{k}'$. The likelihood is then a multivariate Gaussian distribution in the random variables given by the product of the Gaussian distributions of the N bins (Amendola & Tsujikawa 2010):

$$\mathcal{L}(\boldsymbol{\theta}) = \prod_{i=1}^{N}\prod_{l}^{M}\left\{\frac{1}{\sqrt{2\pi}\Delta_{k_l,i}}\exp\left[-\frac{1}{2}\frac{|\delta_{k_l}^{(i)}|^2}{\Delta_{k_l,i}^2}\right]\right\}, \tag{15}$$

where, for simplicity, we have only a set of M discrete wave vectors $\boldsymbol{k}_l$ and where the variance is

$$\Delta_{k_l,i}^2 = V_i\left\langle\delta_{k_l}^{(i)}\delta_{-k_l}^{(i)}\right\rangle + \frac{1}{n_{\rm gal}(z_i)}. \tag{16}$$

The second term in the variance is the shot noise (Seo & Eisenstein 2003), and the coefficients $n_{\rm gal}(z_i)$ are the densities of galaxies in the ith redshift bin, assumed to be constant inside a bin.

The resulting element of the standard Fisher matrix for two parameters θ_α and θ_β is then (Tegmark 1997b; Seo & Eisenstein 2003)

$$F_{\alpha\beta} = \sum_{i=1}^{N}\frac{1}{8\pi^2}\int_{-1}^{1}{\rm d}\mu\int_{k_{\rm min}}^{k_{\rm max}}k^2{\rm d}k\left(\frac{\partial\ln P_{\rm obs}(k,\mu,z_i;\boldsymbol{\theta})}{\partial\theta_\alpha}\frac{\partial\ln P_{\rm obs}(k,\mu,z_i;\boldsymbol{\theta})}{\partial\theta_\beta}\right)V_{\rm eff}^i(k,\mu;\boldsymbol{\theta}), \tag{17}$$

where $P_{\rm obs}$ was given in (11) and

$$V_{\rm eff}^i(k,\mu;\boldsymbol{\theta}) = \left[\frac{n_i P_{\rm obs}(k,\mu,z_i;\boldsymbol{\theta})}{n_i P_{\rm obs}(k,\mu,z_i;\boldsymbol{\theta})+1}\right]^2 f_{\rm sky}V_i. \tag{18}$$

If we want to consider the correlation function given by pairs of galaxies belonging to different redshift bins, the cross-correlation spectra $\sqrt{V_i V_j}\langle\delta_{\boldsymbol{k}}^{(i)}\delta_{-\boldsymbol{k}}^{(j)}\rangle$ for $i \neq j$ need also to be considered and the coefficients $\delta_{\boldsymbol{k}}^{(i)}$ are no longer statistically independent. The cross-correlation spectra represent indeed the off-diagonal elements of the covariance matrix (see Section 3.3 for more details):

$$C_{ij}(\boldsymbol{k}) = \sqrt{V_i V_j}\left\langle \delta_{\boldsymbol{k}}^{(i)}\delta_{-\boldsymbol{k}}^{(j)}\right\rangle + \frac{\delta_{ij}}{n_{\rm gal}(z_i)}. \tag{19}$$

Equation (15) is then rewritten in the form of a Gaussian-correlated distribution for the bins:

$$\mathcal{L}(\boldsymbol{\theta}) = \prod_{l}^{M}\left\{\frac{1}{(2\pi)^{N/2}\sqrt{\det \mathbf{C}(\boldsymbol{k}_l)}}\exp\left[-\frac{1}{2}\sum_{i,j}^{N}\delta_{\boldsymbol{k}_l}^{(i)}\,C_{ij}^{-1}(\boldsymbol{k}_l)\,\delta_{-\boldsymbol{k}_l}^{(i)}\right]\right\}, \tag{20}$$

where bold and capital letters represent $N \times N$ matrices over the bins and we defined the following notation:

$$P_{\rm corr}^{i,j}(\boldsymbol{k}_l) \equiv \sqrt{V_i V_j}\left\langle \delta_{\boldsymbol{k}_l}^{(i)}\delta_{-\boldsymbol{k}_l}^{(j)}\right\rangle. \tag{21}$$

An important remark is that modes at different wave vectors $\boldsymbol{k}_l$ are still assumed independent in equation (20), but the introduction of the window function effects breaks the homogeneity of the density field; thus, this assumption is no longer true. We will discuss this point again in Section 3.3.

The Fisher matrix element in the correlated case then becomes

$$F_{\alpha\beta} = \frac{1}{2}\sum_{i,j,h,g}^{N}\sum_{l}^{M}\frac{\partial P_{\rm corr}^{i,j}(\boldsymbol{k}_l;\boldsymbol{\theta})}{\partial\theta_\alpha}\,C_{jh}^{-1}(\boldsymbol{k}_l)\,\frac{\partial P_{\rm corr}^{h,g}(\boldsymbol{k}_l;\boldsymbol{\theta})}{\partial\theta_\beta}\,C_{gi}^{-1}(\boldsymbol{k}_l) f_{\rm sky}\sqrt[4]{V^i V^j V^h V^g} \tag{22}$$

$$= \frac{1}{8\pi^2}\int_{k_{\rm min}}^{k_{\rm max}}{\rm d}k\,k^2\int_{-1}^{+1}{\rm d}\mu\; f_{\rm sky}{\rm Tr}\left[\frac{\partial\mathbf{P}_{\rm corr}(k,\mu;\boldsymbol{\theta})}{\partial\theta_\alpha}\times\hat{\mathbf{C}}^{-1}(k,\mu)\times\frac{\partial\mathbf{P}_{\rm corr}(k,\mu;\boldsymbol{\theta})}{\partial\theta_\beta}\times\hat{\mathbf{C}}^{-1}(k,\mu)\right], \tag{23}$$

where in the last passage, for convenience, we included the survey comoving volumes in the inverse covariance matrix $\hat{C}_{ij}^{-1}({\rm k},\mu) \equiv C_{ij}^{-1}({\rm k},\mu)\sqrt[4]{V_i V_j}$.

3.2 Redshift as an additional parameter

In Section 3.1, we assumed the redshift-dependent functions $G(z;\boldsymbol{\theta})$, $b(z)$, $f(z;\boldsymbol{\theta})$and$V(z)$ to be constant inside bins and computed them at the median bin redshift. When the bins are wide in redshift, for instance with $\Delta z \approx 0.5$, then this assumption is not a good approximation. To test the impact of this simplification, let us now assign a random variable to the value of the redshift at which we evaluate the redshift-dependent functions. Then, the likelihood in the uncorrelated case becomes

$$\mathcal{L}(\boldsymbol{\theta}) = \prod_{i=1}^{N}\left\{\prod_{l}^{M}\left\{\frac{1}{\sqrt{2\pi}\Delta_{\boldsymbol{k}_l,i}}\exp\left[-\frac{1}{2}\frac{\left|\delta_{\boldsymbol{k}_l}^{(i)}\right|^2}{\Delta_{\boldsymbol{k}_l,i}^2}\right]\right\}\frac{1}{\sqrt{2\pi}\sigma_i}\exp\left[-\frac{1}{2}\frac{(z_i-\hat{z}_i)^2}{\sigma_i^2}\right]\right\}, \tag{24}$$

where, for each bin, z_i are parameters that have a Gaussian distribution centred at the median bin redshift $\hat{z}_i$ and a standard deviation $\sigma_i = \Delta z/6$ equal to one-sixth of the bin redshift width. With this choice, the values of parameters z_i have 99.7 per cent probability to lie within the ith bin, i.e. within the three standard deviations ranges of the probability distribution. This Gaussian distribution can be seen as a prior on the new parameters z_i.

The first part of the likelihood in equation (24) depends on the cosmological parameters and on z_i, whereas the second part depends on the z_i only. The logarithm of the likelihood is

$$-\ln\mathcal{L} = \frac{\ln(2\pi)}{2}(MN+N) + \sum_i\left\{\sum_l \ln\Delta_{\boldsymbol{k}_l,i} + \sum_l\frac{1}{2}\left(\frac{\left|\delta_{\boldsymbol{k}_l}^{(i)}\right|^2}{\Delta_{\boldsymbol{k}_l,i}^2}\right)^2 + \ln\sigma_i + \frac{1}{2}\left(\frac{z_i-\hat{z}_i}{\sigma_i}\right)^2\right\}. \tag{25}$$

The Fisher matrix $\hat{F}_{AB}$ is then an extended version of the old Fisher matrix $F_{\alpha\beta}$ in equation (17), such that A, B are indices ranging from 1 to $N_{\rm cosmo} + 2N$, where N is the number of bins and $N_{\rm cosmo}$ is the number of cosmological parameters.

For A, B ranging from 1 to $N_{\rm cosmo} + N$ (i.e. the cosmological parameters plus one value of bias for each bin), the Fisher matrix $\hat{F}_{AB}$ is equal to F_{AB}. For A, B ranging over $[N_{\rm cosmo} + N + 1, 2N]$, the Fisher matrix elements are

$$\hat{F}_{AB} = \frac{\delta_{AB}}{\sigma_{\hat{A}}^2} + \sum_{i=1}^{N}\frac{1}{8\pi^2}\int_{k_{\rm min}}^{k_{\rm max}}{\rm d}k\,k^2\int_{-1}^{+1}{\rm d}\mu\left(\frac{\partial\ln P_{\rm obs}(k,\mu,z_i;\boldsymbol{\theta})}{\partial z_{\hat{A}}}\frac{\partial\ln P_{\rm obs}(k,\mu,z_i;\boldsymbol{\theta})}{\partial z_{\hat{B}}}\right)V_{\rm eff}^i(k,\mu), \tag{26}$$

where $\hat{A} = A - N_{\rm cosmo} - N - 1$ and $\hat{B} = B - N_{\rm cosmo} - N - 1$. For A ranging over $[N_{\rm cosmo} + N + 1, 2N]$ and B ranging from 1 to $N_{\rm cosmo} + N$, the mixed terms of the Fisher matrix are

$$\hat{F}_{AB} = \sum_{i=1}^{N}\frac{1}{8\pi^2}\int_{k_{\rm min}}^{k_{\rm max}}{\rm d}k\,k^2\int_{-1}^{+1}{\rm d}\mu\left(\frac{\partial\ln P_{\rm obs}(k,\mu,z_i;\boldsymbol{\theta})}{\partial z_{\hat{A}}}\frac{\partial\ln P_{\rm obs}(k,\mu,z_i;\boldsymbol{\theta})}{\partial\boldsymbol{\theta}_B}\right)V_{\rm eff}^i(k,\mu). \tag{27}$$

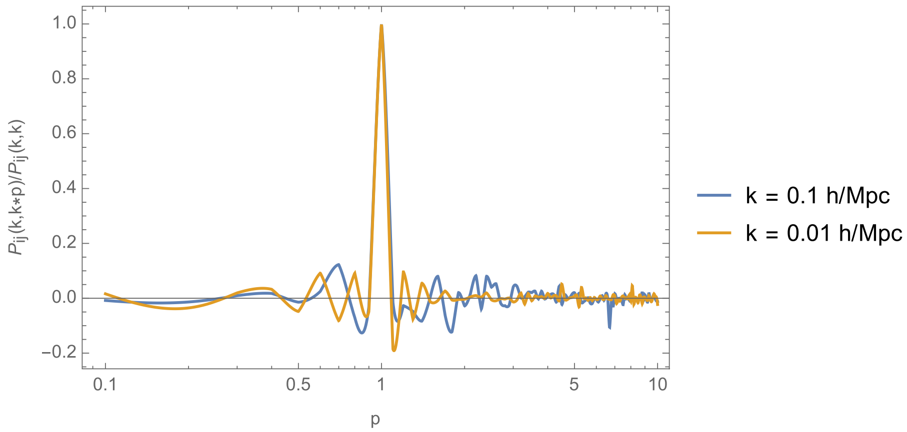

Figure 1. An example of the ratio between expression (31) for $\boldsymbol{k} \neq \boldsymbol{k}'$ and the same expression for $\boldsymbol{k} = \boldsymbol{k'}$. Specifically, the plot shows the ratio between the power spectrum $P_{ij}(\boldsymbol{k}, \boldsymbol{k}') = \sqrt{V_i V_j}\langle \delta_{\boldsymbol{k}}^{(i)} \delta_{-\boldsymbol{k}'}^{(j)} \rangle$ calculated between two contiguous redshift bins (one ranging from $z = 1.05$ to 1.15, and the other ranging from $z = 1.15$ to 1.25, corresponding to two typical central bins for *Euclid*), at values $k = 0.1$ or $0.01\, h\,\mathrm{Mpc}^{-1}$, and $k' = pk$, with p being a dimensionless constant ranging from 0.1 to 10. For both reference values of k, the correlations peak in correspondence of $p = 1$, showing that correlations between different wave vectors are indeed much smaller than those between the same wave vector. The power spectrum used for the calculation has the typical form $\frac{k}{1+k^4}$, and $\boldsymbol{k}'$ is considered to be parallel to $\boldsymbol{k}$ for simplicity, to perform easily the calculations and give a taste of the different magnitudes of the correlations.

Similar calculations lead to corresponding results for the correlated Fisher approach described in equation (22). In Section 5.2, we will show that if we introduce this bin redshift uncertainty, the values of the uncertainties on the cosmological parameters are larger for wider bins in redshift.

3.3 Window function and bin cross-correlation spectra

We now describe the cross-correlation spectrum $P^{i,j}_{\mathrm{corr}}(\boldsymbol{k}_l) \equiv \sqrt{V_i V_j}\langle \delta_{\boldsymbol{k}_l}^{(i)} \delta_{-\boldsymbol{k}_l}^{(j)} \rangle$ introduced previously and the recovery of the standard power spectrum in the limit of an *infinite survey*. Furthermore, we justify the shot-noise term introduced in the covariance matrix (equation 19). With the introduction of the top-hat survey-bin window function $W_i(\boldsymbol{x})$, such that $\int W_i(\boldsymbol{x})\mathrm{d}^3x = V_i$, the coefficients $\delta_{\boldsymbol{k}}^{(i)}$ can be expanded as

$$\delta_{\boldsymbol{k}}^{(i)} = \frac{1}{V_i}\int \delta(\boldsymbol{x}) W_i(\boldsymbol{x}) \mathrm{e}^{-i\boldsymbol{k}\cdot\boldsymbol{x}}\mathrm{d}^3x \tag{28}$$

$$= \frac{1}{V_i}\int \left(\frac{\rho(\boldsymbol{x})}{\rho_0}\right) W_i(\boldsymbol{x}) \mathrm{e}^{-i\boldsymbol{k}\cdot\boldsymbol{x}}\mathrm{d}^3x - \tilde{W}_i(\boldsymbol{k}), \tag{29}$$

where

$$\tilde{W}_i(\boldsymbol{k}) = \frac{1}{V_i}\int W_i(\boldsymbol{x}) \mathrm{e}^{-i\boldsymbol{k}*\boldsymbol{x}}\mathrm{d}^3x. \tag{30}$$

It follows that the cross-correlations between the Fourier coefficients of the density field can be written as (Feldman et al. 1994)

$$\sqrt{V_i V_j}\left\langle \delta_{\boldsymbol{k}}^{(i)} \delta_{-\boldsymbol{k}'}^{(j)} \right\rangle = \frac{\sqrt{V_i V_j}}{(2\pi)^3}\int P(k'')\tilde{W}_i(\boldsymbol{k} - \boldsymbol{k}'')\tilde{W}_j(\boldsymbol{k}' - \boldsymbol{k}'')\mathrm{d}^3k''. \tag{31}$$

This equation shows that this mode–mode correlation (i.e. $\boldsymbol{k} \neq \boldsymbol{k}'$) does not vanish both for $i = j$ and $i \neq j$. Nevertheless, from now on, we will consider correlations only between the same wave vectors, as the ones between different $\boldsymbol{k}$ values lead to more difficult numerical computations and need a new formalization in the Fisher matrix approach. They are in any case smaller than the correlations between the same wave vectors as illustrated in Fig. 1, which justifies our choice.

Correlations between the same wave vectors take the form of a convolution of $P(k)$:

$$\sqrt{V_i V_j}\left\langle \delta_{\boldsymbol{k}}^{(i)} \delta_{-\boldsymbol{k}}^{(j)} \right\rangle = \frac{\sqrt{V_i V_j}}{(2\pi)^3}\int P(k')\tilde{W}_i(\boldsymbol{k} - \boldsymbol{k}')\tilde{W}_j(\boldsymbol{k} - \boldsymbol{k}')\mathrm{d}^3k' \equiv \frac{\sqrt{V_i V_j}}{(2\pi)^3}\int \mathrm{d}^3k'\, P(k')\tilde{Q}_{ij}(\boldsymbol{k} - \boldsymbol{k}'), \tag{32}$$

where $\tilde{Q}_{ij}(\boldsymbol{k}) \equiv \tilde{W}_i(\boldsymbol{k})\tilde{W}_j(\boldsymbol{k})$. This convolution becomes radial when we restrict ourselves to a top-hat spherical window function describing a redshift bin between the comoving distances R_i and $R_i + \Delta_i$. In fact, the Fourier transform of this specific window function is

$$\tilde{W}_i(|\boldsymbol{k}-\boldsymbol{k}'|, R_i, \Delta_i) = \frac{1}{V_i}\int W_i(|\boldsymbol{x}|)\mathrm{e}^{i(\boldsymbol{k}-\boldsymbol{k}')\cdot\boldsymbol{x}}\mathrm{d}^3x \tag{33}$$

$$= \frac{4\pi}{V_i}\int_{R_i}^{R_i+\Delta_i}\frac{\sin\left(|\boldsymbol{k}-\boldsymbol{k}'|x\right)}{|\boldsymbol{k}-\boldsymbol{k}'|x}x^2\mathrm{d}x$$

$$= \frac{4\pi}{V_i}\left[H\left(|\boldsymbol{k}-\boldsymbol{k}'|(R_i+\Delta_i)\right) - H\left(|\boldsymbol{k}-\boldsymbol{k}'|R_i\right)\right], \tag{34}$$

where

$$H(kr) = \frac{\sin kr - kr\cos kr}{k^3}. \tag{35}$$

This shows that the quantity $\tilde{Q}_{ij}(\boldsymbol{k})$ defined in equation (32) will depend only on the modulus of $\boldsymbol{k}$; thus, the convolution becomes radial and the cross-correlation spectra will depend only on the modulus k.

In the limit of an infinite survey, one recovers the standard power spectrum and*vanishing* cross-correlations. In this limit, the window function in Fourier space can indeed be approximated as a Dirac delta; thus, equation (31) with $i = j$ gives the standard (auto)spectrum:

$$V_i\left\langle\delta_k^{(i)}\delta_{-k}^{(i)}\right\rangle = \frac{V_i}{(2\pi)^3V_i^2}\int P(k')\mathrm{e}^{i(\boldsymbol{k}'-\boldsymbol{k})\cdot\boldsymbol{x}}\mathrm{e}^{-i(\boldsymbol{k}-\boldsymbol{k}')\cdot\boldsymbol{y}}\mathrm{d}^3k'\mathrm{d}^3x\mathrm{d}^3y \tag{36}$$

$$= \frac{1}{V_i}\int P(k')\delta_{\mathrm{D}}(\boldsymbol{k}'-\boldsymbol{k})\mathrm{e}^{-i(\boldsymbol{k}-\boldsymbol{k}')\cdot\boldsymbol{y}}\mathrm{d}^3k'\mathrm{d}^3y \tag{37}$$

$$= P(k). \tag{38}$$

Furthermore, in the limit of bins that are far away from each other, the correlation function in equation (31) for $i \neq j$ is computed at large distances $|\boldsymbol{x}-\boldsymbol{y}|$ where its value is close to zero. Thus, in this limi,t we find vanishing correlations $\sqrt{V_iV_j}\left\langle\delta_{\boldsymbol{k}}^{(i)}\delta_{-\boldsymbol{k}'}^{(j)}\right\rangle$ (see equation 31).

Finally, we derive the shot-noise term introduced in the covariance matrix in equation (20). So far we analysed a continuum field, but for a galaxy survey, we should rather consider a discrete distribution of N_i particles located at positions $\boldsymbol{x}_l$ inside the ith bin. From equation (29), we rewrite the Fourier coefficients as

$$\delta_{\boldsymbol{k}}^{(i)} = \frac{1}{V_i}\int\frac{\sum_l\delta_{\mathrm{D}}(\boldsymbol{x}-\boldsymbol{x}_l)}{\rho_0}W_i(\boldsymbol{x})\mathrm{e}^{-i\boldsymbol{k}\cdot\boldsymbol{x}}\mathrm{d}^3x - \tilde{W}_i(\boldsymbol{k})$$

$$= \frac{1}{N_i}\sum_l W_i(\boldsymbol{x}_l)\mathrm{e}^{-i\boldsymbol{k}\cdot\boldsymbol{x}_l} - \tilde{W}_i(\boldsymbol{k}), \tag{39}$$

and since $\langle\delta(k)\rangle = 0$, we have

$$\frac{1}{N_i}\left\langle\sum_l W_i(\boldsymbol{x}_l)e^{-i\boldsymbol{k}\cdot\boldsymbol{x}_l}\right\rangle = \tilde{W}_i(\boldsymbol{k}). \tag{40}$$

The cross-correlations are then

$$\sqrt{V_iV_j}\left\langle\delta_k^{(i)}\delta_{-k}^{(j)}\right\rangle = \sqrt{V_iV_j}\left\langle\left(\frac{1}{N_i}\sum_l W_i(\boldsymbol{x}_l)\mathrm{e}^{-i\mathbf{k}\cdot\boldsymbol{x}_l} - \tilde{W}_i(\boldsymbol{k})\right)\left(\frac{1}{N_j}\sum_m W_j(\boldsymbol{x}_m)e^{+i\mathbf{k}\cdot\boldsymbol{x}_m} - \tilde{W}_j(-\boldsymbol{k})\right)\right\rangle \tag{41}$$

$$= \frac{\delta_{ij}V_i}{N_i} + \frac{\sqrt{V_iV_j}}{N_iN_j}\left\langle\sum_{l\neq m}W_i(\boldsymbol{x}_l)W_j(\boldsymbol{x}_m)e^{-i\mathbf{k}\cdot(\boldsymbol{x}_l-\boldsymbol{x}_m)}\right\rangle - \sqrt{V_iV_j}\tilde{W}_i(\boldsymbol{k})\tilde{W}_j(-\boldsymbol{k}) \tag{42}$$

$$\equiv \delta_{ij}P_N + P_{\mathrm{filtered}}(k) - P_W(k). \tag{43}$$

This coincides with the previous result except for the shot noise $P_N = V_i/N_i = 1/n_{\mathrm{gal}}(z_i)$. As we can note, this term is not present for cross-correlation spectra between different bins.

4 NUMERICAL EVALUATION OF THEORETICAL OBSERVED WINDOWED SPECTRA AND OBSERVED BIN CROSS-CORRELATION SPECTRA

In this section, we analyse how the redshift distortions modify the cross-correlation spectra and we tune the parameters of the radial FFT algorithm based on three toy-model forms of power spectra for which the convolution integral can be solved analytically. Assuming a linear power spectrum, we now introduce the redshift distortions given by equation (9) in the cross-correlation spectra, similarly to what we did in Section 2. If we assume that quantities $G(z;\boldsymbol{\theta})$, $b(z)$and $f(z;\boldsymbol{\theta})$ are scale independent as we did previously, equation (11) can then be generalized as

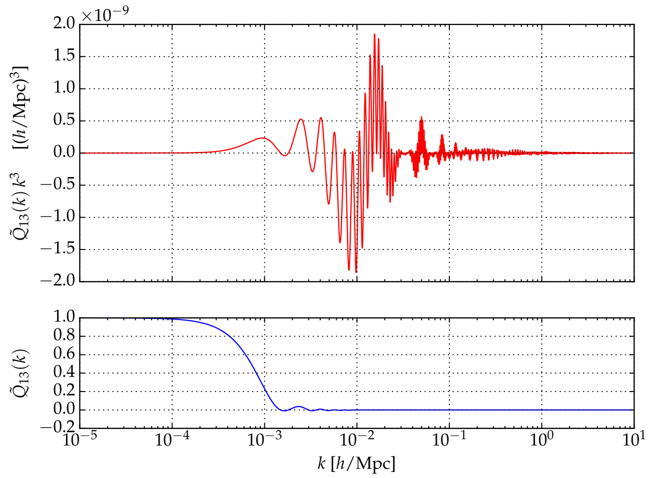

Figure 2. We consider the first and third bins of *Euclid* (Table 1). We plot $\tilde{Q}_{13}(k)$ (blue plot) and $\tilde{Q}_{13}(k)k^3$ (red plot), as defined in equation (32). The integrand of the logarithmic version of the integral in equation (46) is proportional to $\tilde{Q}_{13}(k)k^3$ multiplied by the power spectrum $P(k)$. The plot of this rapidly oscillating integrand gives an idea of why it is hard to integrate it accurately.

$$P_{\rm obs}(k,\mu,z_i,z_j;\boldsymbol{\theta}) = \sigma_8^2 b(z_i)b(z_j)\sqrt{\left[\frac{H(z_i;\boldsymbol{\theta}')\cdot D_{\rm A}^2(z_i;\boldsymbol{\theta})}{H(z_i;\boldsymbol{\theta})\cdot D_{\rm A}^2(z_i;\boldsymbol{\theta}')}\right]\left[\frac{H(z_j;\boldsymbol{\theta}')\cdot D_{\rm A}^2(z_j;\boldsymbol{\theta})}{H(z_j;\boldsymbol{\theta})\cdot D_{\rm A}^2(z_j;\boldsymbol{\theta}')}\right]} \times\left[1+\beta(z_i;\boldsymbol{\theta}')\mu^2\right]\left[1+\beta(z_j;\boldsymbol{\theta}')\mu^2\right]\mathscr{P}_{\rm conv}(k,z_i,z_j;\boldsymbol{\theta}'), \tag{44}$$

where we defined the convolved spectrum $\mathscr{P}_{\rm conv}(k;z_i,z_j;\boldsymbol{\theta}')$ as

$$\mathscr{P}_{\rm conv}(k,z_i,z_j;\boldsymbol{\theta}') \equiv G(z_i;\boldsymbol{\theta})G(z_j;\boldsymbol{\theta})\frac{\sqrt{V_iV_j}}{(2\pi)^3}\int {\rm d}^3k'\,P(k',z=0;\boldsymbol{\theta}')\tilde{Q}_{ij}(|\boldsymbol{k}-\boldsymbol{k}'|) \tag{45}$$

to make the relation with equation (11) evident. Note that we neglected the shot noise $P_{\rm s}(z_i)$ because its contribution proved to be negligible with large survey bins (e.g. in the Euclid survey).

In the last two formulae, we neglected the AP effect on the modulus k, the cosine μ, the volumes of the shells in $\mathscr{P}_{\rm conv}(k,z_i,z_j;\boldsymbol{\theta}')$ and the shell radii R_i entering the window functions (equation 34). The only AP effect considered in equations (44) and (45) is the effect on the volume over which the power spectra are computed. In Appendix B, we study the complete AP effect. As explained in Appendix B, we simplified equation (B13) to make the computations less time-consuming.

The convolution in equation (32) is solved numerically and the integral can also be written as a double one:

$$\sqrt{V_iV_j}\left\langle\delta_k^{(i)}\delta_{-k}^{(j)}\right\rangle = \frac{\sqrt{V_iV_j}}{(2\pi)^3}\int_0^\infty {\rm d}k'k'^2P(k)\int_{-1}^1{\rm d}\Omega\,\tilde{Q}_{ij}(\sqrt{k^2+k'^2-2kk'\Omega}). \tag{46}$$

Numerical quadrature algorithms for solving integrals of this type are time-consuming and require high precision to reach convergence. The function $\tilde{Q}_{ij}(k)$ in the argument of the integral is indeed a rapidly oscillating function, which is hard to integrate accurately (Fig. 2). A radial FFT algorithm (Appendix A) is then used for solving the radial convolution in equation (45).

As a test of the numerical accuracy, we can solve analytically the integral in equation (46) by considering three toy-model forms of power spectra. Then, we compare the analytical results with the ones obtained by using the radial FFT algorithm so that we can calibrate the cut-off in the wavelengths and the number of samplings (called, respectively, $\mathcal{R}$ and $\mathcal{N}$ in equations A8 and A9 of Appendix A).

Let us first assume a constant spectrum $P(k)=\mathcal{C}$. Then, the convolution is equal to $\mathcal{C}$ for $i=j$ and is zero for $i\neq j$:

$$\sqrt{V_iV_j}\left\langle\delta_k^{(i)}\delta_{-k}^{(j)}\right\rangle = \frac{\mathcal{C}}{(2\pi)^3\sqrt{V_iV_j}}\int {\rm d}^3k'{\rm d}^3x{\rm d}^3y\,W_i(|\boldsymbol{x}|)W_j(|\boldsymbol{y}|){\rm e}^{i(\boldsymbol{k}')\cdot(\boldsymbol{x}+\boldsymbol{y})}{\rm e}^{i(\boldsymbol{k})\cdot(\boldsymbol{x}+\boldsymbol{y})} \tag{47}$$

$$= \frac{\mathcal{C}}{\sqrt{V_iV_j}}\int {\rm d}^3x{\rm d}^3y\,W_i(|\boldsymbol{x}|)W_j(|\boldsymbol{y}|)\delta_{\rm D}(\boldsymbol{x}+\boldsymbol{y}){\rm e}^{i(\boldsymbol{k})\cdot(\boldsymbol{x}+\boldsymbol{y})} \tag{48}$$

$$= \mathcal{C}\delta_{ij}, \tag{49}$$

where we assumed that different bins do not overlap. Then, we consider other two toy-model forms of spectrum:

$$P_A(k) \equiv \begin{cases}10^4({\rm Mpc}/h)^3 & k\in[0.05,0.2]h/{\rm Mpc}\\ 0 & \text{otherwise,}\end{cases} \qquad P_B(k) \equiv \begin{cases}10^4({\rm Mpc}/h)^3 & k\in[0,0.2]h/{\rm Mpc}\\ 0 & \text{otherwise.}\end{cases} \tag{50}$$

In the limit $k\to 0$, the double integral in equation (46) can be solved analytically for these two window spectra. After a proper tuning of the parameters, we have seen that the choice of the parameters $\mathcal{N}=7000$ and $\mathcal{R}=1.5\ h\ {\rm Mpc}^{-1}$ leads to percentage differences below

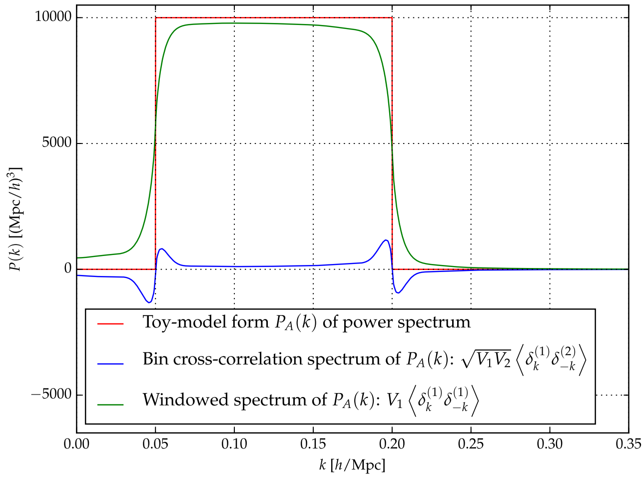

Figure 3. A toy-model form $P_A(k)$ (red plot) of the power spectrum is considered: $P_A(k) = 10^4$ (Mpc $h^{-1})^3$ for $k \in [0.05, 0.2]$ h Mpc^{-1} and 0 otherwise. We consider the first and second bins of *Euclid* (Table 1). The green and the blue plots represent $V_1\left\langle \delta_k^{(1)}\delta_{-k}^{(1)}\right\rangle$ and $\sqrt{V_1 V_2}\left\langle \delta_k^{(1)}\delta_{-k}^{(2)}\right\rangle$, respectively (see equation 46). They are computed using a radial FFT algorithm with parameters $\mathcal{N} = 7000$, $\mathcal{R} = 1.5$ h Mpc^{-1} (Appendix A).

Table 1. Specifications of the Euclid survey: 14 bins from redshift 0.65 to 2.05 with depth $\Delta z = 0.1$ (Laureijs et al. 2011; Amendola et al. 2013). For each bin, the table lists the redshift ranges, the average redshift, the galaxy density and the fiducial values of the bias. The number density of galaxies $n(z)$ is estimated using the latest empirical data (see table 3 in Amendola et al. 2013 and fig. 3.2 in Laureijs et al. 2011). We follow the commonly employed procedure in galaxy clustering Fisher matrix forecasts, such that within each bin, the galaxy density $n(z_i)$ is assumed to be constant (see Seo & Eisenstein 2003; Amendola et al. 2005; Wang 2006; Albrecht et al. 2009; Di Porto et al. 2012; Wang 2012; Xu et al. 2014).

Bin's redshift range	Average redshift	Density $n(z_i) \cdot 10^{-3}$	Bias $b(z_i)$
0.65–0.75	$z_1 = 0.7$	1.25	1.30
0.75–0.85	$z_2 = 0.8$	1.92	1.34
0.85–0.95	$z_3 = 0.9$	1.83	1.38
0.95–1.05	$z_4 = 1.0$	1.68	1.41
1.05–1.15	$z_5 = 1.1$	1.51	1.45
1.15–1.25	$z_6 = 1.2$	1.35	1.48
1.25–1.35	$z_7 = 1.3$	1.20	1.52
1.35–1.45	$z_8 = 1.4$	1.00	1.55
1.45–1.55	$z_9 = 1.5$	0.80	1.58
1.55–1.65	$z_{10} = 1.6$	0.58	1.61
1.65–1.75	$z_{11} = 1.7$	0.38	1.64
1.75–1.85	$z_{12} = 1.8$	0.35	1.67
1.85–1.95	$z_{13} = 1.9$	0.21	1.70
1.95–2.05	$z_{14} = 2.0$	0.11	1.73

0.3 per cent, when we compare the analytical solution with the numerical results. Thus, we conclude that those values of $\mathcal{N}$ and $\mathcal{R}$ represent a good compromise between the accuracy and the computational time. Finally, Fig. 3 shows the windowed version of the toy-model window spectrum $P_A(k)$ and the cross-correlation spectrum of $P_A(k)$ for the first and the second *Euclid* bins, computed using the FFT algorithm with the chosen parameters. We repeated the same exercise with a more realistic shape of the power spectrum $\frac{k}{1+(k/k_0)^4}$, finding similarly good results, which confirms the goodness of our choice of $\mathcal{N}$ and $\mathcal{R}$.

Now that the parameters of the radial FFT algorithm have been tuned, they can be used to solve the convolution in equation (45). Thus, we can then compute the observed cross-correlation spectra in equation (44) and the correlated Fisher matrix in equation (23). In the next section, we describe the results for the probability distributions of the cosmological parameters.

5 TESTING THE ASSUMPTIONS: RESULTS

We will now test the assumptions regarding the effect of the window function, the bin cross-correlations and the bin redshift uncertainty. In particular, we focus on the future survey of the *Euclid* mission. Survey specifications are listed in Table 1.

Given the windowed and cross-correlation spectra computed with the radial FFT algorithm as described in Section 4, we analyse the probability distributions of the cosmological parameters using the Fisher matrix approach described in Section 3.1 with the following set of cosmological parameters:

$$\boldsymbol{\theta} = \{h, n_s, \Omega_b^{(0)}, \Omega_{cdm}^{(0)}, w_0, \sigma_8\}. \quad (51)$$

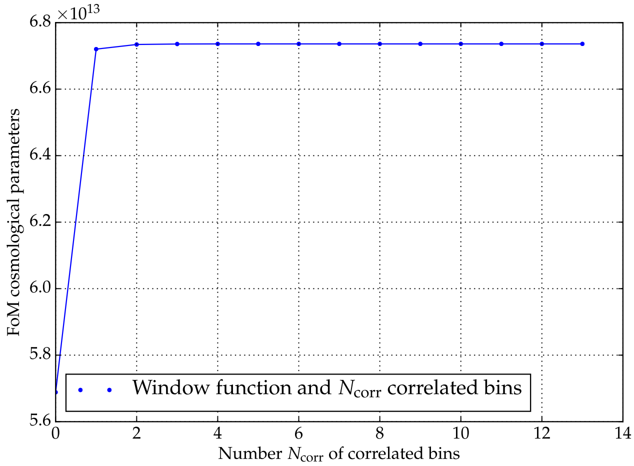

Figure 4. FoM for all the cosmological parameters as a function of the number $N_{\rm corr}$ of cross-correlated bins ($N_{\rm corr} = 0$ means no cross-correlation, $N_{\rm corr} = 1$ means that only the cross-correlations between contiguous bins are considered, etc.). All the bias coefficients are marginalized over. We consider the redshift range of the *Euclid* mission with 14 bins (Table 1). The window function effect is included. The bin redshift uncertainty and the AP effect are not considered.

The fiducial values of the cosmological parameters are taken from the *Planck* results (Planck Collaboration XIII 2016). Since the bias function is undefined, along with the parameters above, we add a bias parameter for each bin and marginalize over it (Seo & Eisenstein 2003). Fiducial values b_i for the bias parameters are shown in Table 1. The values of $k_{\rm max}$ and $k_{\rm min}$ in equation (17) and (23) that we used for computing the Fisher matrix are $5 \cdot 10^{-3}$ and 0.2 $h\,{\rm Mpc}^{-1}$, respectively. We also experimented a value of the maximum k equal to $0.15h\,{\rm Mpc}^{-1}$, finding similar results to the ones we present here: The increase in the marginalized errors on the cosmological parameters averages around 6 per cent, with a maximum increase of 15 per cent. *Our implementation of the Fisher matrix is available publicly. The power spectra were computed using the open source software* CAMB *(Lewis, Challinor & Lasenby 2000).*

To analyse the probability distributions of the cosmological parameters, we quantify the following (1) the fully marginalized 1σ uncertainties on each of the parameters, given by $\sigma(\theta_\alpha) = \sqrt{\left(\mathbf{F}^{-1}\right)_{\alpha\alpha}}$; (2) the marginalized confidence contour regions for pairs of parameters; and (3) the figure of merit (FoM) for all the combined cosmological parameters, defined as

$$\mathrm{FoM} \equiv \sqrt{\det \mathbf{F}}, \tag{52}$$

which is inversely proportional to the area of the marginalized confidence contour regions.

5.1 Euclid survey

Since computing bin correlations for each pair of bins is computationally expensive, particularly with the complete AP effect (Appendix B), it is desirable to reduce the number of considered pairs. We tested how good is the approximation to consider only the correlations between contiguous bins. In Fig. 4, we plot the FoM values computed with bin correlations for neighbouring pairs of bins, so that the number of neighbours $N_{\rm corr}$ is given by the horizontal axis, i.e. if the number of correlated bins is equal to 1, then bin correlations are computed for contiguous bins only; if the number of correlated bins is equal to 13, then bin correlations are computed for all pairs of bins. The figure shows that the FoM values do not increase with an increasing number of bins beyond the nearest neighbour when the bin size is $\Delta z = 0.1$. Thus, we can conclude that it is sufficient to focus on nearby bins, and in the following, we consider correlations only among bins closer than $\Delta z = 0.1$. Note that in our analysis, we neglected the lensing effect. By adding it, we expect the correlation terms to become more important and we are currently working on it. As shown in (Montanari & Durrer 2015, Fig. 2), the lensing effect modifies mainly the correlations between distant bins, which, in our analysis, are neglected because of their small contribution to the final constraints.

For each parameter, Table 3 contains the fiducial values of the cosmological parameters (column 1), the values of the marginalized 1σ uncertainties computed without neither the window function effect nor bin correlations (columns 2 and 3), the values of the uncertainties computed with only the window function (columns 4 and 5) and the values of the uncertainties computed with the window function and bin correlations (columns 6 and 7). In columns 4–7, we also provide the percentages of the differences of the corresponding values to the values in columns 2 and 3. All computations were done with and without considering the AP effect (Section 4 and Appendix B) and with respect to the *Euclid* specifications (Table 1).

As shown in Table 3, the window function has a significant effect (15–38 per cent difference from the case without the window function) on parameters h, $n_{\rm s}$, $\Omega_{\rm b}^{(0)}$and$\Omega_{\rm cdm}^{(0)}$. Table 3 also shows that adding bin correlations reduces the uncertainties for all considered parameters as compared to the case with only the window function. There is still a significant difference on parameters h, $n_{\rm s}$, $\Omega_{\rm b}^{(0)}$and$\Omega_{\rm cdm}^{(0)}$ (12–30 per cent) as compared to the case without neither the window function nor bin correlations.

Table 3 shows that the complete AP effect has a considerable influence on the uncertainties of parameters $\Omega_{\rm cdm}^{(0)}$, $w_0$andσ_8. The results are also shown in Figs 5 and 6. As explained in Appendix B, we simplified equation (B13) to make the computations less time-consuming. Even

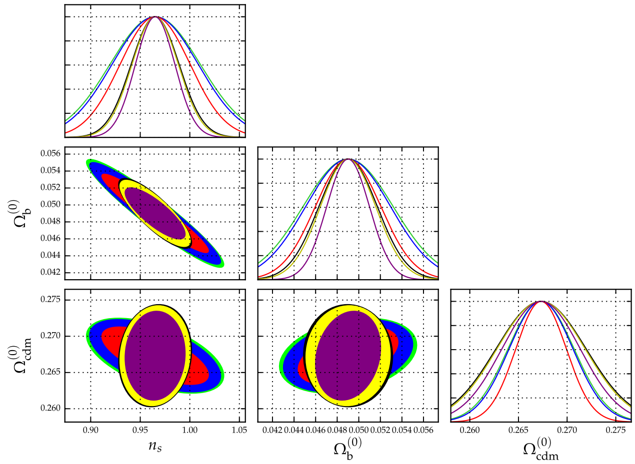

Figure 5. Marginalized confidence contour regions (1σ contours) for pairs of cosmological parameters n_s, $\Omega_b^{(0)}$ and $\Omega_{cdm}^{(0)}$ with and without the AP effect computed towards the *Euclid* specifications (Table 1). The red, green and blue ellipses are computed without the AP effect (Section 4 and Appendix B). The purple, black and yellow ellipses are computed with the AP effect. The red and purple ellipses are computed without neither the window function nor bin correlations; the green and black ones include the effect of the window function; and the blue and yellow ones include both the correlations and the window function. We consider only correlations between contiguous bins. We also show the 1D probability distributions for each considered parameter.

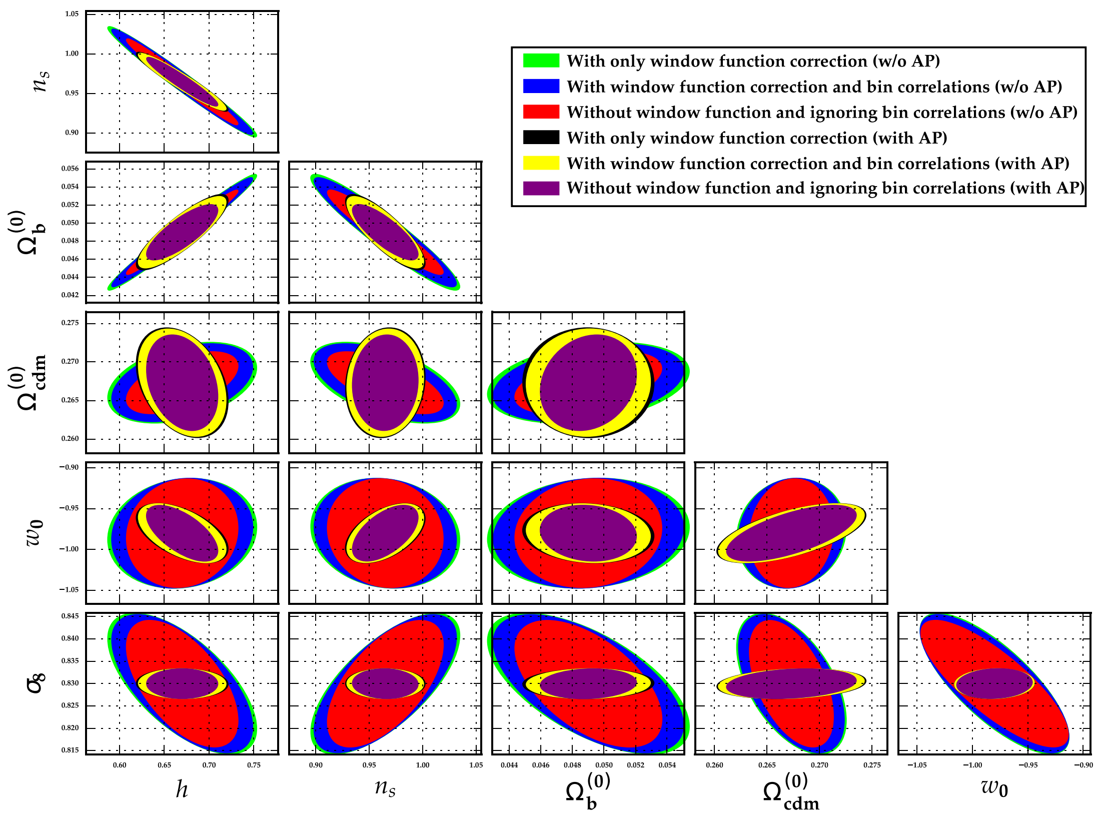

Figure 6. Same as Fig. 5, but for pairs of all the considered cosmological parameters. The 1D probability distributions are omitted.

with the simplified equation (B13), the processing runtime is orders of magnitude larger as compared to the runtime without the AP effect and by using FFT algorithms. Thus, ignoring the AP effect significantly reduces the runtime when the window function or bin correlations are considered.

In Table 3, we consider the redshift of the bins as an additional parameter. The differences in the values computed without considering the redshift as an additional parameter are significant only for the parameters σ_8 and w_0 (12–18 per cent difference).

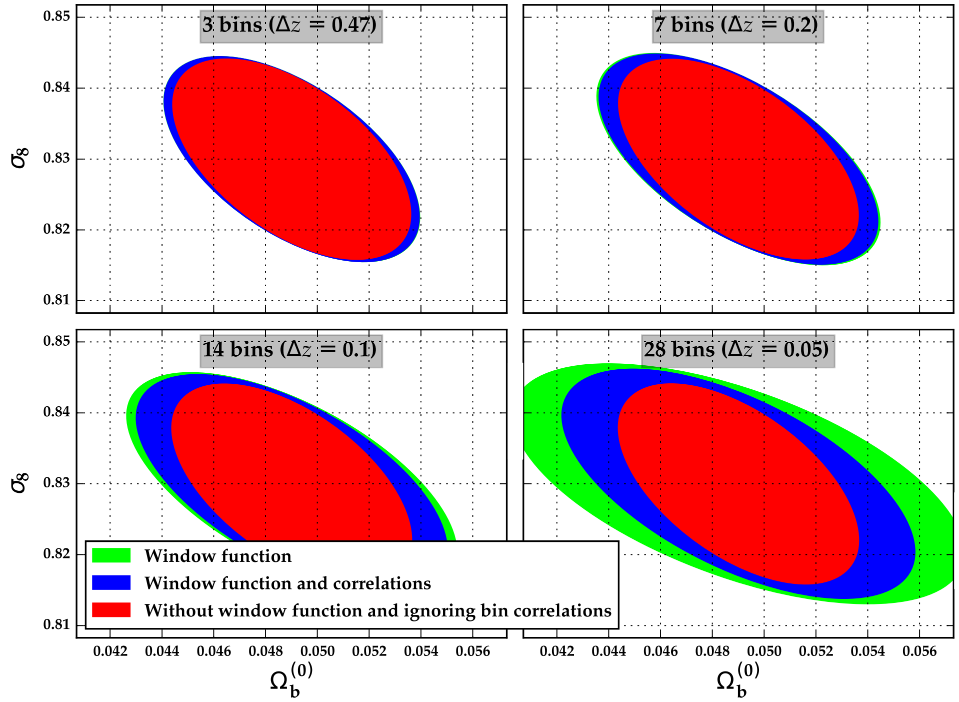

Figure 7. Marginalized confidence contour regions for σ_8 and $\Omega_{\rm b}^{(0)}$ (1σ contours) for different numbers of bins. The red ellipses are computed using a Fisher matrix approach without considering the window function effect and cross-correlations between bins. The green ellipses are computed with the window function. The blue ellipses are computed with the window function and correlations between bins. The AP effect is neglected.

5.2 Varying number of bins

We test the effects of the assumptions with respect to the number of bins. We consider the redshift range of the *Euclid* mission, $z \in [0.65, 2.05]$ (see Table 1). We subdivide this range into N bins and vary N in range from 2 to 95. The galaxy density $n(z_i)$ at a redshift z_i is still assumed to be constant inside the bin. For a number of bins different from the standard 14 bins considered for the *Euclid* mission, the values $n(z_i)$ and $b(z_i)$ are found by performing a fit of the values shown in Table 1. As explained in Section 5.1, since computing bin correlations for each pair of bins (here maximum 4465 pairs) is computationally expensive, it is desirable to reduce the number of considered pairs. For a *Euclid* with 14 bins, we concluded that it is sufficient to focus on the contiguous bins. Since the width of a *Euclid* bin is equal to $\Delta z = 0.1$, in the following, we compute always correlations for contiguous bins if the distance between bin boundaries is $\Delta z \geq 0.1$ and among all the bins closer than $\Delta z = 0.1$ if the bins are smaller than 0.1. Then, for instance, with $N = 20$, the distance between two contiguous bins is $\Delta z_{\rm bins} = 0.07$; thus, we consider correlations between bins i, $i \pm 1$and$i \pm 2$.

Fig. 8 shows the dependence of the FoM (equation 52) on the number of bins for all combined cosmological parameters in equation (51). The red plot is computed using the Fisher matrix without considering neither the window function effect nor cross-correlations between bins. The green plot is computed with just the window function effect, and the blue plot is computed with the window function effect and bin correlations. Fig. 7 shows the marginalized confidence contour regions for σ_8 and $\Omega_{\rm b}^{(0)}$ for different number of bins. The other parameters are marginalized over. The red ellipses are computed using the Fisher matrix without considering the window function effect and cross-correlations between bins. The green ellipses are computed with only the window function. The blue ellipses are computed with the window function and correlations between bins. Based on these figures, we analyse the effects of the window function and the bin correlations. In both Figs 7 and 8, redshift is not considered as an additional parameter; thus, there is no uncertainty on the value of the redshift bins.

No bin cross-correlations, no window function effect: As mentioned in Section 3.1, without bin cross-correlations, the random variables assigned to Fourier coefficients $\{\delta_k^{(1)}, \ldots, \delta_k^{(N)}\}$ are statistically independent. If we increase N, one would expect smaller uncertainties on the parameters $\boldsymbol{\theta}$ (equation 51). However, Fig. 8 (red curve) shows that the value of the FoM (equation 52) does not significantly vary with increasing number of bins because the volume factor $V_{\rm i}$ (equation 18) compensates the increased value of N.[4] In other words, we consider more bins but the amount of information we obtain from each of them is less. Similarly, in Fig. 7, red ellipses have a similar shape for different number of bins.

Window function effect without bin cross-correlations: We now test the effects of the window function and consider the observed convolved power spectrum in equation (44) for $i = j$. Fig. 7 shows that green ellipses are larger for a larger number of bins. Similarly, the

[4] Note that the Fisher matrix element (equation 17) does not significantly vary, but it is not constant. The reason is that all the spectra are computed at the median bin redshifts and these values vary for different number of bins.

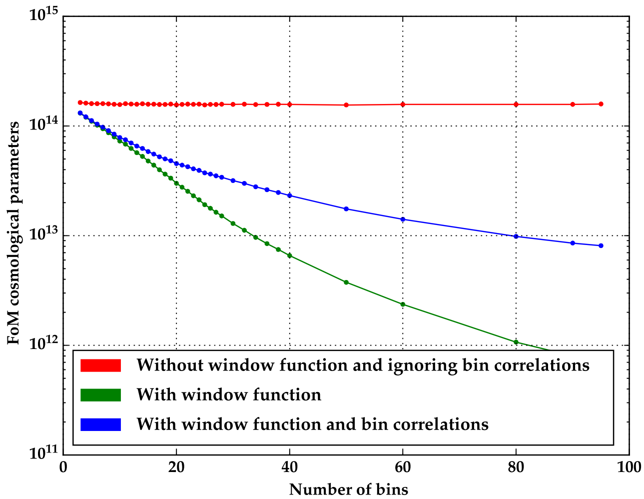

Figure 8. FoM for all the cosmological parameters as a function of the number of bins. All the bias coefficients are marginalized over. We consider the redshift range of the *Euclid* mission. The red plot is computed without considering neither the window function effect nor cross-correlations between bins. The green plot is computed with just the window function effect, and the blue plot is computed with the window function effect and bin correlations. For the case with correlations (blue plot), we compute bin correlations only for the bin pairs such that the distance between the bins is less than Δz =0.1

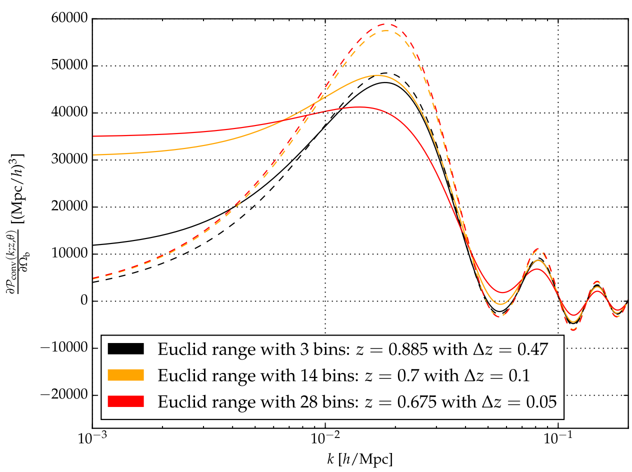

Figure 9. Derivatives with respect to parameter $\Omega_{\rm b}^{(0)}$ of the convolved spectrum in equation (45) (solid lines) and the standard linear spectrum in equation (8) (dashed lines) for different number of bins. We consider the redshift range of the *Euclid* mission. We subdivide this range into 3, 14 and 28 bins (black, orange and red plots, respectively). Note that for increasing number of bins, in the region of $k \in [10^{-2}, 10^{-1}]\ h\ \mathrm{Mpc}^{-1}$, the values of the convolved derivatives are smaller with respect to the derivatives of the standard linear spectra.

FoM in Fig. 8 (green plot) decreases with an increasing number of bins. Thus, the window function results in larger uncertainties for a larger number of bins.

This effect can be also seen in Fig. 9, which shows the derivatives with respect to parameter $\Omega_{\rm m}^{(0)}$ of the convolved spectrum (equation 45) and the standard linear spectrum (equation 8) for different number of bins. Note that for an increasing number of bins, in the region of $k \in [10^{-2}, 10^{-1}]\ h\ \mathrm{Mpc}^{-1}$, the values of the convolved derivatives are smaller with respect to the derivatives of the standard linear spectra. Thus, with the window function effect, the spectrum derivatives in equation (17) have smaller values and a Fisher matrix with smaller values corresponds to larger uncertainties.

Bin cross-correlations and window function effect: We now test the second assumption and consider correlations between different bins. Fig. 7 shows that uncertainties with only the window function (green ellipses) are larger as compared to the ones with bin correlations and window function (blue ellipses). The figure also shows that adding bin correlations decreases the uncertainties for a larger number of bins as compared to the case with only the window function. The same effect can be seen in Fig. 8, where the FoM values with only window function (green plot) decrease more as compared to the values with both the window function and bin correlations (blue plot). In the case with both the window function and bin correlations, note that the values of the FoM (blue plot) decrease slowly for a larger number of bins, but the FoM does not reach a constant value as one would expect. We conjecture that, for a large number of bins, neglecting the mode–mode correlations for $\boldsymbol{k} \neq \boldsymbol{k}'$ decreases the values of the FoM.

Redshift as an additional parameter: In section 3.2, we considered the redshift of the bins as an additional parameter. Fig. 10 shows the FoM computed by using Fisher matrix $\hat{F}_{AB}$ (Section 3.2) marginalized over redshift parameters z_i and bias parameters b_i. Note that for a

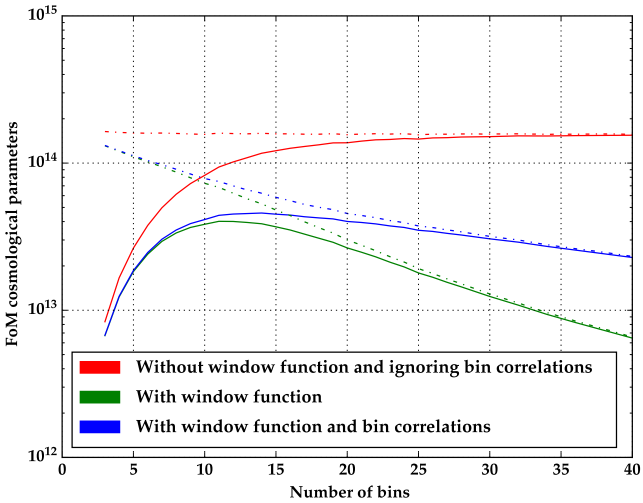

Figure 10. Same as Fig. 8, now including the bin redshift uncertainty (solid lines), compared with the case without considering the window function effect and cross-correlations (dashed lines).

Table 2. For each parameter, the table contains the fiducial values of the cosmological parameters (column 1), the values of the marginalized 1σ uncertainties computed without neither the window function effect nor bin correlations (columns 2 and 3), the values of the uncertainties computed with only the window function (columns 4 and 5) and the values of the uncertainties computed with the window function and bin correlations between contiguous bins (columns 6 and 7). In columns 4–7, we also provide the percentages of the differences of the corresponding values to the values in columns 2 and 3. All computations were done with and without considering the AP effect (Section 4 and Appendix B) and with respect to the *Euclid* specifications (Table 1).

	Fiducial values	Parameters uncertainties without window function correction and ignoring bin correlations		Parameters uncertainties considering only the window function correction		Parameters uncertainties with the window function correction and bin cross-correlations	
		Without AP	With AP	Without AP	With AP	Without AP	With AP
h	0.67	0.041	0.026	0.054 (+34 per cent)	0.033 (+29 per cent)	0.051 (+27 per cent)	0.032 (+23 per cent)
n_s	0.965	0.035	0.020	0.045 (+29 per cent)	0.024 (+22 per cent)	0.043 (+23 per cent)	0.023 (+17 per cent)
$\Omega_b^{(0)}$	0.049	0.0030	0.0020	0.0042 (+38 per cent)	0.0027 (+37 per cent)	0.0039 (+30 per cent)	0.0026 (+29 per cent)
$\Omega_{cdm}^{(0)}$	0.2673	0.0026	0.0040	0.0034 (+31 per cent)	0.0046 (+15 per cent)	0.0033 (+26 per cent)	0.0045 (+12 per cent)
w_0	−0.98	0.043	0.022	0.044 (+1.0 per cent)	0.023 (+6.5 per cent)	0.044 (+1 per cent)	0.0233 (+5.7 per cent)
σ_8	0.83	0.0092	0.0021	0.0103 (+11 per cent)	0.0021 (+0 per cent)	0.0101 (+9 per cent)	0.0021 (+0 per cent)

small number of bins, the values of the FoM are smaller as compared to the values of the FoM shown in Fig. 8. Thus, if we consider the redshifts of the bins as parameters, this results in larger uncertainties on the cosmological parameters for a smaller number of bins. In the case with the window function and bin correlations, the values of the uncertainties present a maximum for 14 bins, which is usually the number considered for the Euclid survey (Table 1). For $N \gtrsim 25$, the values of the FoM computed with and without redshift as an additional parameter are close to each other, i.e. the addition of the bin-redshift uncertainty do not modify the results. We also experimented with another value of the standard deviation σ_i (equation 24) equal to half of the bin width. With this increased bin-redshift uncertainty, the values of the FoM are smaller than compared to the one shown in Fig. 10 and in the case with the window function and bin correlations (blue plot), the maximal value of the FoM reaches around ∼25 bins.

6 CONCLUSIONS

Forecast studies for galaxy clustering mostly rely on the Fisher matrix method and typically imply several assumptions, including neglecting the window function effect and the bin cross-correlation spectra, and fixing the bin redshift range to the median value. In this paper, we proposed an approach for testing if these assumptions hold for realistic surveys, in particular, the Euclid survey, and we estimated the change on the parameter forecast. We also investigated the dependence of the effects on the number of redshift bins and included the AP effect in a simplified form. For computations, we used an FFT algorithm and implemented an optimized Fisher matrix. The main results of this paper are summarized in Tables 2 and 3. The results suggest that the window function and the bin cross-correlations, although acting in opposite sense, have a considerable combined influence on the forecasted errors for a Euclid-like survey, amounting to 10–30 per cent for several of the cosmological parameters.

Table 3. For each parameter, the table contains the fiducial values of the cosmological parameters (column 1), the values of the marginalized 1σ uncertainties computed without neither the window function effect nor bin correlations (columns 2 and 3), the values of the uncertainties computed with only the window function (columns 4 and 5) and the values of the uncertainties computed with the window function and bin correlations between contiguous bins (columns 6 and 7). In columns 3, 5 and 7, we also provide the percentages of the differences between the values with and without bin redshift uncertainty. All computations were done without considering the AP effect (Section 4 and Appendix B) and with respect to the *Euclid* specifications (Table 1).

	Fiducial values	Parameters uncertainties without window function correction and ignoring bin correlations		Parameters uncertainties considering only the window function correction		Parameters uncertainties with the window function correction and bin cross-correlations	
		Without redshift parameters	with redshift parameters	Without redshift parameters	with redshift parameters	Without redshift parameters	with redshift parameters
h	0.67	0.041	0.041 (−per cent)	0.054	0.054 (−per cent)	0.051	0.051 (−per cent)
n_s	0.965	0.035	0.035 (−per cent)	0.045	0.046 (−per cent)	0.043	0.043 (−per cent)
$\Omega_b^{(0)}$	0.049	0.0030	0.0030 (−per cent)	0.0042	0.0042 (−per cent)	0.0039	0.0039 (−per cent)
$\Omega_{cdm}^{(0)}$	0.2673	0.0026	0.0026 (−per cent)	0.0034	0.0034 (−per cent)	0.0033	0.0033 (−per cent)
w_0	−0.98	0.043	0.051 (+18 per cent)	0.044	0.051 (+17 per cent)	0.044	0.051 (+17 per cent)
σ_8	0.83	0.0092	0.011 (+14 per cent)	0.0103	0.012 (+12 per cent)	0.0101	0.011 (+12 per cent)

Possible improvements of our approach that we will pursue in future work include the following: First, the dependence of the survey volume and k_{max} and k_{min} in equation (17) on the cosmological parameters can be considered. A second possible improvement concerns a further optimization of the algorithm for computing the derivatives of the convolved spectra with the AP effect, which proved to be computationally expensive in our study. Thirdly, further models besides ΛCDM should be considered. Fourthly, whereas we considered only the linear power spectrum, non-linearities could also be taken into consideration. Fifthly, we plan to assess the impact of the mode–mode correlation, so far neglected in most analyses. We expect it to be particularly important for small bins. Finally, other approximations that need to be tested and to be improved upon are the flat-sky redshift distortion and the neglect of large-scale relativistic effects like lensing.

ACKNOWLEDGEMENTS

We would like to thank Katya Ovchinnikova and Santiago Casas for their various contributions that made this paper possible, and Ruth Durrer, Daniele Bertacca for useful discussions. This research has been supported by DFG through the grant TRR33 'The Dark Universe'. ASM acknowledges financial support from the graduate college *Astrophysics of cosmological probes of gravity* by Landesgraduiertenakademie Baden-Württemberg.

REFERENCES

Albrecht A. et al., 2009, preprint (arXiv:0901.0721)
Alcock C., Paczyński B., 1979, Nature, 281, 358
Amendola L., Tsujikawa S., 2010, Dark Energy: Theory and Observations. Cambridge Univ. Press, Cambridge
Amendola L., Quercellini C., Giallongo E., 2005, MNRAS, 357, 429
Amendola L. et al., 2013, Living Rev. Relativ., 16, 6
Baumgart D. J., Fry J., 1991, ApJ, 375, 25
Bonaldi A., Harrison I., Camera S., Brown M. L., 2016, MNRAS, 463, 3686
DESI Collaboration 2016, The Dark Energy Spectroscopic Instrument (DESI), available at http://desi.lbl.gov/
Di Porto C., Amendola L., Branchini E., 2012, MNRAS, 423, L97
Dodelson S., 2003, Modern Cosmology. Academic press, San Diego, CA
eBOSS Collaboration 2016, The extended Baryon Oscillation Spectroscopic Survey (eBOSS), available at http://www.sdss.org/surveys/eboss/
Feldman H. A., Kaiser N., Peacock J. A., 1994, ApJ, 426, 23
Fisher R. A., 1935, J. R. Stat. Soc., 98, 39
Fisher K. B., Scharf C. A., Lahav O., 1994, MNRAS, 266, 219
Flaugher B., 2005, Int. J. Mod. Phys. A, 20, 3121
Groth E. J., Peebles P., 1977, ApJ, 217, 385
Heavens A., 2009, preprint (arXiv:0906.0664)
Heavens A., Taylor A., 1995, MNRAS, 275, 483
Hill G. J. et al., 2008, in Kodama T., Yamada T., Aoki K., eds, ASP Conf. Ser. Vol. 399, Panoramic Views of Galaxy Formation and Evolution. Astron. Soc. Pac., San Francisco, p. 115
Kaiser N. et al., 2002, Proc. SPIE, 4836, 154
Lahav O., Lilje P., Primack J., Rees M., 1991, MNRAS, 251, 128
Laureijs R. et al., 2011, preprint (arXiv:1110.3193)
Lewis A., Challinor A., Lasenby A., 2000, ApJ, 538, 473
Linder E. V., 2005, Phys. Rev. D, 72, 043529
LSST Science Collaboration et al., 2009, preprint (arXiv:0912.0201)
Lyth D. H., Liddle A. R., 2009, The Primordial Density Perturbation: Cosmology, Inflation and the Origin of Structure. Cambridge Univ. Press, Cambridge
Montanari F., Durrer R., 2012, Phys. Rev. D, 86, 063503

Montanari F., Durrer R., 2015, J. Cosmol. Astropart. Phys., 2015, 070
Peebles P., 1976, ApJ, 205, 318
Peebles P., 1980, The Large-Scale Structure of the Universe. Princeton Univ. Press, Princeton, NJ
Planck Collaboration XIII, 2016, A&A, 594, A13
Polarski D., Gannouji R., 2008, Phys. Lett. B, 660, 439
Press W. H., 2007, Numerical Recipes, 3rd edn. Cambridge Univ. Press, Cambridge
Raccanelli A., Bertacca D., Jeong D., Neyrinck M. C., Szalay A. S., 2016, preprint (arXiv:1602.03186)
Schlegel D. et al., 2011, preprint (arXiv:1106.1706)
Seo H.-J., Eisenstein D., 2003, ApJ, 598, 720
Tegmark M., 1997a, Phys. Rev. D, 55, 5895
Tegmark M., 1997b, Phys. Rev. Lett., 79, 3806
Tegmark M., Taylor A. N., Heavens A. F., 1997, ApJ, 480, 22
Trotta R., 2008, Contemp. Phys., 49, 71
Wang Y., 2006, ApJ, 647, 1
Wang Y., 2012, MNRAS, 423, 3631
Wang L., Steinhardt P. J., 1998, ApJ, 508, 483
Xu Y., Wang X., Chen X., 2014, ApJ, 798, 40
Yahya S., Bull P., Santos M. G., Silva M., Maartens R., Okouma P., Bassett B., 2015, MNRAS, 450, 2251
Yu J., Peebles P., 1969, ApJ, 158, 103

APPENDIX A: FFT ALGORITHM FOR A RADIAL CONVOLUTION

In this appendix, we explain how to use a 1D FFT algorithm to solve a radial convolution integral like the one in equation (45). For the solution of the integral in equation (45), FFT algorithms are orders of magnitude faster and more precise in comparison to numerical quadrature algorithms.

A radial convolution integral has the following expression:

$$c(x) = \int f(|\boldsymbol{x}'|)g(|\boldsymbol{x} - \boldsymbol{x}'|)\mathrm{d}^3x'. \tag{A1}$$

The goal is to use a 1D FFT algorithm to find the Fourier transform and inverse transform of a radial function like $f(|\boldsymbol{x}|)$ and then use the convolution theorem. Thus, for any radial function $f(|\boldsymbol{x}|)$, we have

$$\tilde{f}(k) = \frac{4\pi}{k}\int_0^\infty f(r)\sin(kr)r\mathrm{d}r, \tag{A2}$$

$$f(r) = \frac{1}{(2\pi)^3}\frac{4\pi}{r}\int_0^\infty \tilde{f}(k)\sin(kr)k\mathrm{d}k. \tag{A3}$$

Compared to the usual FFT methods, the sine functions are defined on the whole positive real axis. Thus, we need to assume to deal with functions that are zero beyond some cut-off distance $\mathcal{R}$. We also assume that $f(r+\mathcal{R}) = f(r)$ and we discretize

$$k_l = \frac{\pi}{\mathcal{R}}l \qquad\qquad r_n = \frac{\mathcal{R}}{\mathcal{N}}n, \tag{A4}$$

with $n, l \in \{0, \ldots, \mathcal{N}-1\}$. We proceed by defining $F_n \equiv r_n f(r_n)$ and $\tilde{F}_l \equiv k_l \tilde{f}(k_l)$. Then, it can be shown that

$$\mathcal{S}(F_n) \equiv \tilde{F}_l = 2\sum_{n=0}^{\mathcal{N}-1} F_n \sin\left(\frac{\pi}{\mathcal{N}}nl\right) = -\mathrm{Im}\left[\sum_{n=0}^{M-1} \bar{F}_n \exp\left(-i\frac{2\pi}{M}nl\right)\right], \tag{A5}$$

$$\mathcal{S}^{-1}(\tilde{F}_l) \equiv F_n = \frac{1}{\mathcal{N}}\sum_{l=0}^{\mathcal{N}-1} \tilde{F}_l \sin\left(\frac{\pi}{\mathcal{N}}nl\right) = -\frac{1}{2\mathcal{N}}\mathrm{Im}\left[\sum_{n=0}^{M-1} \bar{\tilde{F}}_l \exp\left(-i\frac{2\pi}{M}nl\right)\right], \tag{A6}$$

where we defined $M = 2\mathcal{N}$ and the extended coefficients (similar for $\bar{\tilde{F}}_l$)

$$\bar{F}_n \equiv \begin{cases} F_n & 0 \le n < \mathcal{N} \\ 0 & n = \mathcal{N} \\ -F_{2\mathcal{N}-n} & \mathcal{N} < n \le 2\mathcal{N}-1. \end{cases} \tag{A7}$$

In this way, for computing $\mathcal{S}$ and $\mathcal{S}^{-1}$, we can just apply a normal 1D FFT algorithm on the new defined coefficients and then take the imaginary part of it.

Considering all the coefficients and the cases with $k_l = 0$ or $n = 0$, the final results for the radial and inverse transforms are

$$\tilde{f}_l = \begin{cases} \frac{\mathcal{R}}{\pi k_l}\mathcal{S}\left[f_n \frac{n\mathcal{R}}{\mathcal{N}}\right] & k_l \neq 0 \\ 2\sum_{n=0}^{\mathcal{N}-1} f_n \left(\frac{n\mathcal{R}}{\mathcal{N}}\right)^2 & k_l = 0, \end{cases} \tag{A8}$$

$$f_n = \begin{cases} \frac{\mathcal{N}}{n\mathcal{R}}\mathcal{S}^{-1}\left[\tilde{f}_l \frac{\pi l}{\mathcal{R}}\right] & n \neq 0 \\ \frac{1}{\mathcal{N}}\sum_{l=0}^{\mathcal{N}-1}\tilde{f}_l\left(\frac{\pi l}{\mathcal{R}}\right)^2 & n = 0. \end{cases} \quad \text{(A9)}$$

We can now use the formula (A8) to compute the discrete Fourier transform of the radial functions $f(|\boldsymbol{x}|)$ and $g(|\boldsymbol{x}|)$. Then, we apply the convolution theorem to (A1), i.e. $\tilde{c}(k) = \tilde{f}(k)\tilde{g}(k)$, and we use (A9) to find $c(x)$.

APPENDIX B: THE AP EFFECT ON THE WINDOWED SPECTRA

In this appendix, we will study how to include the AP effect on the modulus k, the cosine μ, the volumes of the shells in equation (45) and the shell radii R_i in the window functions. To do so, we need to decompose $\boldsymbol{k}$ in $\boldsymbol{k}_{||} + \boldsymbol{k}_{\perp}$ along the line of sight. By changing the cosmological parameters, the two components of $\boldsymbol{k}$ transform as

$$\boldsymbol{k}_{\perp}^{(2)} = \boldsymbol{k}_{\perp}^{(1)}\frac{D_{\mathrm{A}}(z;\boldsymbol{\theta}_1)}{D_{\mathrm{A}}(z;\boldsymbol{\theta}_2)} = \boldsymbol{k}_{\perp}^{(1)}\alpha(z), \qquad \boldsymbol{k}_{||}^{(2)} = \boldsymbol{k}_{||}^{(1)}\frac{H(z;\boldsymbol{\theta}_2)}{H(z;\boldsymbol{\theta}_1)} = \boldsymbol{k}_{||}^{(1)}\gamma(z), \quad \text{(B1)}$$

where we hid the dependence of $\alpha(z)$ and $\gamma(z)$ on the sets of cosmological parameters $\boldsymbol{\theta}_1$ and $\boldsymbol{\theta}_2$ for a simpler notation. The scale vector $\boldsymbol{x}$ will transform in similar way with reciprocal quantities, so that the inner product $\boldsymbol{k}\cdot\boldsymbol{x}$ is invariant under a parameter transformation. In the following, we will use the simplified notations

$$\boldsymbol{k}_2 = \boldsymbol{k}_{\perp}^{(1)}\alpha(z) + \boldsymbol{k}_{||}^{(1)}\gamma(z) \equiv \mathbf{U}(z)\,\boldsymbol{k}_1, \qquad \boldsymbol{x}_2 \equiv \mathbf{U}^{-1}(z)\,\boldsymbol{x}_1, \quad \text{(B2)}$$

where $\mathbf{U}(z)$ is a matrix depending on z. For volumes and modules of the vectors, we have

$$\mathrm{d}^3x_2 = \mathrm{d}^3x_1\frac{H(z;\boldsymbol{\theta}_1)D_{\mathrm{A}}^2(z;\boldsymbol{\theta}_2)}{H(z;\boldsymbol{\theta}_2)D_{\mathrm{A}}^2(z;\boldsymbol{\theta}_1)} \equiv \mathrm{d}^3x_1\zeta(z), \qquad \mathrm{d}^3k_2 = \frac{\mathrm{d}^3k_1}{\zeta(z)}, \quad \text{(B3)}$$

$$k_2 = \Upsilon(z)k_1, \qquad x_2 = \frac{x_1}{\Upsilon(z)}, \quad \text{(B4)}$$

where $\Upsilon(z)$ was defined in equation (14). We can now include the previously mentioned AP effects in equation (31). We start with $i = j$ and $\boldsymbol{k} = \boldsymbol{k}'$:

$$\left[V_i\left\langle\delta^{(i)}_{U_i\boldsymbol{k}}\delta^{(i)}_{-U_i\boldsymbol{k}}\right\rangle\right]_{\mathrm{AP}} = \frac{\zeta_i V_i}{(2\pi)^3}\int \mathrm{d}^3k' P(k')\tilde{W}^2_{i,\mathrm{AP}}\left[\mathbf{U}_i\boldsymbol{k} - \mathbf{U}_i\boldsymbol{k}'\right] \quad \text{(B5)}$$

$$= \frac{V_i}{(2\pi)^3}\int \mathrm{d}^3k' P(\Upsilon_i k')\tilde{W}^2_{i,\mathrm{AP}}\left[U_i\boldsymbol{k} - U_i\boldsymbol{k}'\right], \quad \text{(B6)}$$

where we changed the integral variable $\boldsymbol{k}'_{\mathrm{old}} = \mathbf{U}_i\boldsymbol{k}'_{\mathrm{new}}$ so the Jacobian will be $\mathrm{d}^3k'_{\mathrm{old}} = \mathrm{d}^3k'_{\mathrm{new}}/\zeta_i$ and the integral is computed over all the space so the substitution does not affect that. By defining the modified window function $W_{i,\mathrm{AP}}(x/\Upsilon_i) \equiv W_i(x)$, we note that the Fourier window function computed in a shifted vector $\mathbf{U}_i\boldsymbol{k}$ is just $\tilde{W}_i(\boldsymbol{k})$:

$$\tilde{W}_{i,\mathrm{AP}}(\mathbf{U}_i\boldsymbol{k}) = \frac{1}{\zeta_i V_i}\int W_{i,\mathrm{AP}}(x)\mathrm{e}^{i\,\mathbf{U}_i\boldsymbol{k}\cdot\boldsymbol{x}}\mathrm{d}^3x \quad \text{(B7)}$$

$$= \frac{1}{V_i}\int W_{i,\mathrm{AP}}(x/\Upsilon_i)\mathrm{e}^{i\boldsymbol{k}\cdot\boldsymbol{x}}\mathrm{d}^3x \quad \text{(B8)}$$

$$= \tilde{W}_i(\boldsymbol{k}), \quad \text{(B9)}$$

where we changed again the variable in the second passage ($\boldsymbol{x}_{\mathrm{old}} = \mathbf{U}_i^{-1}\boldsymbol{x}_{\mathrm{new}}$). By considering now the full convolved spectrum defined in equation (45), we can conclude that the full derivative with respect to the cosmological parameters[5] is

$$\frac{\mathrm{d}\ln\mathscr{P}^{\mathrm{conv}}_{ii}}{\mathrm{d}\theta_\alpha}(k,\mu,z_i;\boldsymbol{\theta}) = \frac{1}{\mathscr{P}^{\mathrm{conv}}_{ii}}G_i^2\frac{V_i}{(2\pi)^3}\left[\int \mathrm{d}^3k'\frac{\partial P(k',z=0;\boldsymbol{\theta})}{\partial\theta_\alpha}\tilde{W}_i^2(|\boldsymbol{k}-\boldsymbol{k}'|) + \int \mathrm{d}^3k'\frac{\partial P(k',z=0;\boldsymbol{\theta})}{\partial k'}\frac{\partial k'}{\partial\theta_\alpha}(k',\mu',z_i;\boldsymbol{\theta})\tilde{W}_i^2(|\boldsymbol{k}-\boldsymbol{k}'|)\right] + 2\frac{\partial\ln G(z_i;\boldsymbol{\theta})}{\partial\theta_\alpha}. \quad \text{(B10)}$$

The integral in the second term[6] is no longer a radial convolution. Thus, we need a 3D FFT algorithm to solve it, but for this specific integral, this method is too memory-consuming. Then, we used a quadrature algorithm to solve the integral. Note that with a change of the integration variable (k', ϕ', ψ') such that ϕ' becomes the angle between $\boldsymbol{k}$ and $\boldsymbol{k}'$, the angular integral in ψ' can be solved analytically.

[5] The derivative formalized here needs to be computed to find the Fisher matrix (equation 23).

[6] If we consider the cosmological parameters used for our computation of the Fisher matrix (equation 51), then we note that the first term of equation (B10) is non-zero for $\theta_\alpha \in \{h, n_{\mathrm{s}}, \Omega_{\mathrm{b}}^{(0)}, \Omega_{\mathrm{cdm}}^{(0)}, w_0\}$; instead, the second and third ones are non-zero only for $\theta_\alpha \in \{\Omega_{\mathrm{b}}^{(0)}, \Omega_{\mathrm{cdm}}^{(0)}, w_0\}$.

The AP effect on the cross-correlation spectra leads to more difficulties. For different bins $i \neq j$, we note that $\boldsymbol{k}$ and $\boldsymbol{k}'$ in equation (31) change differently for a transformation of the cosmological parameters. Thus, we cannot fix $\boldsymbol{k} = \boldsymbol{k}'$ as we did in equation (B5) or (32) because we would compute a correlation term between different modes $\mathbf{U}_i\boldsymbol{k}$ and $\mathbf{U}_j\boldsymbol{k}$, which have been neglected in this paper. Then, we rather fix the transformed modes to be equal, i.e. $\mathbf{U}_i\boldsymbol{k} = \mathbf{U}_j\boldsymbol{k}'$, and with similar steps, we find that

$$\left[\sqrt{V_i V_j}\left\langle \delta^{(i)}_{\mathbf{U}_i\boldsymbol{k}}\delta^{(j)}_{-\mathbf{U}_i\boldsymbol{k}}\right\rangle\right]_{\rm AP} = \frac{\sqrt{\zeta_i V_i \zeta_j V_j}}{(2\pi)^3}\int P(k')\tilde{W}_{i,\rm AP}[\mathbf{U}_i\boldsymbol{k} - \boldsymbol{k}']\tilde{W}_{j,\rm AP}[\mathbf{U}_i\boldsymbol{k} - \boldsymbol{k}']{\rm d}^3k' \tag{B11}$$

$$= \frac{\sqrt{\zeta_i V_i \zeta_j V_j}}{(2\pi)^3}\int P(k')\tilde{W}_i\left[\boldsymbol{k} - \mathbf{U}_i^{-1}\boldsymbol{k}'\right]\tilde{W}_j\left[\mathbf{U}_i\mathbf{U}_j^{-1}\left(\boldsymbol{k} - \mathbf{U}_i^{-1}\boldsymbol{k}'\right)\right]{\rm d}^3k' \tag{B12}$$

$$= \frac{\sqrt{V_i V_j}}{(2\pi)^3}\sqrt{\frac{\zeta_j}{\zeta_i}}\int P(\Upsilon_i k')\tilde{W}_i\left[\boldsymbol{k} - \boldsymbol{k}'\right]\tilde{W}_j\left[\mathbf{U}_i\mathbf{U}_j^{-1}\left(\boldsymbol{k} - \boldsymbol{k}'\right)\right]{\rm d}^3k', \tag{B13}$$

where, again in the last passage, we changed the variable ($\boldsymbol{k}'_{\rm old} = \mathbf{U}_i\boldsymbol{k}'_{\rm new}$). We see that this result generalizes the previous one given by equations (B5) and (B7) for $i = j$, but in the same way, we could have computed the correlation at $\mathbf{U}_j\boldsymbol{k}$ and we would have found a different result for equation (B13).[7]

To compute the plots in Figs 5 and 6 and the data listed in Table 2, we have done the following approximations on the AP effect. Double integrals solved with quadrature algorithms are time-consuming; thus, for *Euclid,* we considered correlations only between adjacent bins. As explained in Section 5.1 by the results without AP effect, this represents a good approximation. For adjacent bins, we approximate $\mathbf{U}_i\boldsymbol{k} \approx \mathbf{U}_j\boldsymbol{k}$; thus, this solves the problem described previously. Furthermore, we note that in equation (B13), it is no longer possible to change the integration variable and solve analytically the integral in ψ'. Quadrature algorithms for triple integrals are too time-consuming; then, we approximate the factor $\mathbf{U}_i\mathbf{U}_j^{-1} \approx \mathbb{1}$ in equation (B13), i.e. we consider the same AP correction on both the window functions $W_i(\boldsymbol{x})$ and $W_j(\boldsymbol{x})$.

We considered these approximations to show that the effects of the window function and of the bin correlations remain similar when we add the AP effect (Table 3, and Figs 5 and 6). Nevertheless, the computations of the windowed spectra with the AP effect are orders of magnitudes slower compared to the ones computed without it. Thus, we conclude that the addition of the window function or bins correlations does not increase computational times only without including the AP effect.

[7] This is equivalent to fixing the condition $U_j\boldsymbol{k} = U_i\boldsymbol{k}'$. Note indeed that if $\boldsymbol{k} = \boldsymbol{k}'$, then the correlation $\langle\delta^{(i)}_{\boldsymbol{k}}\delta^{(j)}_{-\boldsymbol{k}}\rangle$ is symmetric for an exchange of the bins i and j, but for $\boldsymbol{k} \neq \boldsymbol{k}'$, then $\langle\delta^{(i)}_{\boldsymbol{k}}\delta^{(j)}_{-\boldsymbol{k}'}\rangle \neq \langle\delta^{(j)}_{\boldsymbol{k}}\delta^{(i)}_{-\boldsymbol{k}'}\rangle$ (see equation 31).

This paper has been typeset from a TEX/LATEX file prepared by the author.